

GRAVITATIONAL WAVE ASTRONOMY*

Jordan B. Camp¹ and Neil J. Cornish²

¹Laboratory for High Energy Astrophysics, Goddard Space Flight Center,
Greenbelt, Maryland 20771; email: Jordan.B.Camp@nasa.gov

²Department of Physics, Montana State University, Bozeman, Montana 59717;
email: cornish@physics.montana.edu

Key Words gravitational radiation, black holes, general relativity

PACS Codes 04.30.–Db, 95.30.SF, 95.55.YM

■ **Abstract** The existence of gravitational radiation is a direct prediction of Einstein's theory of general relativity, published in 1916. The observation of gravitational radiation will open a new astronomical window on the universe, allowing the study of dynamic strong-field gravity, as well as many other astrophysical objects and processes impossible to observe with electromagnetic radiation. The relative weakness of the gravitational force makes detection extremely challenging; nevertheless, sustained advances in detection technology have made the observation of gravitational radiation probable in the near future. In this article, we review the theoretical and experimental status of this emerging field.

CONTENTS

1. INTRODUCTION TO GRAVITATIONAL WAVES	526
1.1. History of Field	527
1.2. Physics of Gravitational Waves	530
1.3. Basic Analysis Concepts	534
2. SOURCES: MODELS, STRENGTHS, AND RATES	536
2.1. Source Modeling	536
2.2. Extremely Low Frequency (10^{-18} Hz to 10^{-15} Hz)	537
2.3. Very Low Frequency (10^{-9} Hz to 10^{-7} Hz)	537
2.4. Low Frequency (10^{-4} Hz to 1 Hz)	538
2.5. High Frequency (10^1 Hz to 10^4 Hz)	543
3. MEASUREMENT TECHNIQUES	547
3.1. Experimental Noise Sources	547
3.2. Requirements and Principles of Detectors	549
3.3. Descriptions of Facilities	552
3.4. Planned Facility Upgrades	558
4. DATA ANALYSIS	560

*The U.S. Government has the right to retain a nonexclusive, royalty-free license in and to any copyright covering this paper.

4.1. Data-Analysis Techniques	560
4.2. Ground-Based Interferometer Results	563
4.3. Resonant Mass Detector (Bar) Results	569
4.4. Doppler Tracking Results	570
4.5. Pulsar Timing Results	571
4.6. Space-Based Interferometer Analysis	572
5. CONCLUSIONS	573

1. INTRODUCTION TO GRAVITATIONAL WAVES

The detection and study of gravitational waves have the potential to revolutionize our understanding of the universe. Gravitational radiation arises in regions of strong and dynamical gravitational fields from astronomical or cosmological sources. Its character describes the nature of gravity in the extreme, testing the predictions of Einstein's theory of gravity and providing information about its sources unobtainable through other means. In contrast to the electromagnetic waves of conventional astronomy, which arise from the incoherent superposition of emission from the acceleration of individual electric charges, gravitational waves result from coherent, bulk motions of matter. Also, because gravitational waves interact only weakly with matter they are able to penetrate the very densely concentrated matter that produces them. In contrast, emerging electromagnetic waves are strongly scattered and attenuated by intervening matter. Whereas electromagnetic waves offer a surface impression of their astronomical source—the surface of last scattering—gravitational waves cut to the (high-density) core.

Among the wealth of new insights in both physics and astrophysics that the study of gravitational waves will bring are:

- Direct confirmation of the existence of black holes, including a test of the fundamental “no-hair” theorem
- Tests of general relativity under extreme strong-field conditions
- Measurement of the propagation speed of the graviton
- Detailed information on the properties of neutron stars, including the equation of state
- Insights into the earliest stages of the evolution of the universe through the measurement of primordial gravitational waves
- Studies of galactic merging through the observation of coalescing massive black holes at their centers

Finally, because strong gravitational wave sources are so different in character from strong photon sources, the potential for discovering new and unanticipated astronomical phenomena is high.

In this article, we describe the present status of the emerging field of gravitational wave astronomy. Section 1 gives a brief history of the theoretical and experimental development of the field and introduces the physics of gravitational waves. In Section 2 we describe anticipated gravitational wave sources, and in Section 3 we

describe the experimental techniques and facilities that will attempt their detection. Section 4 summarizes the data-analysis efforts to date.

1.1. History of Field

This brief introduction to the development of the field of gravitational radiation includes both theory and experimental efforts.

1.1.1. THEORY In the early part of the twentieth century, Albert Einstein embarked on a course of theoretical activity that greatly impacted our understanding of the physical world. He was guided by the motivation to express physical law in a form that was independent of the reference frame of the observer; in so doing, he showed that the classical Newtonian viewpoint of the absolute nature of space and time was inadequate.

In his special theory of relativity (1), Einstein postulated two principles: All inertial observers are equivalent, and the velocity of light c is the same in all inertial reference frames. The consequence of these two postulates was the redefinition of space and time in accordance with the Lorentz transformations:

$$\begin{aligned}x' &= \gamma(x - vt) \\t' &= \gamma(t - vx/c^2)\end{aligned}$$

where $\gamma = 1/(1 - v^2/c^2)^{1/2}$ and (x, t) and (x', t') are coordinates measured in inertial frames moving with relative velocity v . The experimental predictions of this theory, from time dilation (moving clocks appear to run slowly) to the equivalence of mass and energy, have been extensively tested and in all cases found to be in excellent agreement with theory.

Special relativity addressed the nature of space and time, the stage on which other physics, such as electromagnetism, thermodynamics, hydrodynamics, etc., plays its role. Shortly after the formulation of special relativity, however, Einstein realized that gravity could not be accommodated within the framework of special relativity because of the apparent equivalence of gravitational and inertial mass. Elevating the equivalence of gravitational and inertial mass to the status of a fundamental physical principle—the equivalence principle—led Einstein to an understanding of gravity as the physical manifestation of curvature in the geometry of space-time. In this new theory, aptly named general relativity, space-time curvature is associated with the stress-energy tensor of matter fields:

$$G_{\mu\nu} = 8\pi G_N T_{\mu\nu}. \quad 1.$$

In this equation $G_{\mu\nu}$ is the so-called Einstein tensor, which is formed from the Ricci curvature tensor and the space-time metric $g_{\mu\nu}$; $T_{\mu\nu}$ is the stress-energy tensor of matter fields; and G_N is Newton's gravitational constant. Though simple in appearance, the Einstein tensor is a nonlinear function of the metric and its first and second derivatives; this very compact geometrical statement hides 10 coupled, nonlinear partial differential equations for the metric. In the Einstein field equations, matter tells space-time how to curve, but the curved space-time also tells matter how to move (2). This dual role for the Einstein equations—as

both field equations and equations of motion—is unique among classical field theories and is the source of many of the difficulties one encounters in describing the interaction of massive bodies. At lowest order, the field equations imply that matter follows geodesics of the space-time manifold (3, 4).

The form of general relativity we know today was published by Einstein in 1916 (5). In that work he described wavelike solutions to the linearized equations of the theory. Soon after the publication of the theory, Schwarzschild published a solution to the vacuum equations in the special case of spherical symmetry, which described space-time and gravity outside a spherically symmetric star. The solution also described the curious situation of a spherically symmetric gravitational “field” without any matter source at all and with singular curvature at the center. The Schwarzschild solution remained a poorly understood curiosity until the late 1960s, when its relevance as an endpoint in stellar evolution began to be appreciated and the name “black hole” was coined to describe the solution and its generalizations (to include angular momentum and electric charge).

In 1918 Einstein expanded on his initial work with a calculation of the energy carried by gravitational waves (6). The question of the physicality of the waves—whether they carry energy or are instead a “gauge” effect—would remain controversial into the 1960s. Eddington showed that the wave solutions to the linearized equations included pure gauge solutions and correctly identified the physical degrees of freedom, while also noting that the linearized equations were inadequate for treating wave sources, such as binary star systems, where gravity itself plays a significant role in the source structure. Einstein himself seriously questioned the physicality of gravitational waves in the mid 1930s (7). Landau & Lifshitz presented an influential calculation of the effect of gravitational radiation emission on a binary star system in their textbook *Classical Theory of Fields* (8). The uncertain state of the radiation problem in general relativity attracted the attention of a new community of theoretical physicists, notably Bondi, in the 1950s. Bondi was influenced by a calculation by Pirani (9) that showed that gravitational waves would exert tidal forces on intervening matter, producing a strain in the material with a quadrupole oscillation pattern. The question of whether the waves were physical was settled rather quickly; however, the correctness of the calculation, and, in particular, whether the results obtained from the linearized theory were correct to leading order for the nonlinear theory, remained matters of controversy into the 1980s. These issues would ultimately be settled by the observation of the radiation-driven decay of the Hulse-Taylor binary pulsar system in accord with the predictions of the linearized theory (10). (For an overall history of the radiation problem in general relativity, see Reference 11.)

1.1.2. EXPERIMENT The history of the experimental search for gravitational radiation begins with the work of Weber (12). Stimulated by predictions of the possibility of earth-incident gravitational waves with amplitude of order 10^{-17} at frequencies near 1 kHz, Weber set out to build a detector sufficiently sensitive to observe them. His idea was to use an aluminum bar 2 m in length and 0.5 m in diameter,

whose resonant mode of oscillation (~ 1.6 kHz) would overlap in frequency with the incoming waves (12). The bar, built at the University of Maryland, was fitted with piezo-electric transducers to convert its motion to an electrical signal, and it provided a strain sensitivity of order 10^{-15} over millisecond time scales. In 1971, with the coincident use of similar detectors in Illinois, Weber claimed detection of gravitational waves from the direction of the galactic center (13). Although he insisted on the correctness of his data, many attempts to independently reproduce this finding were unsuccessful, and Weber remained a controversial figure until his death in 2001. Nevertheless, Weber is rightly credited with undertaking the first real experimental effort in the search for gravitational radiation, and demonstrating that experimental sensitivity to motion at a level much smaller than a nuclear diameter is feasible.

With the increasing theoretical confidence that gravitational wave strains were likely to be of the order of 10^{-21} or less and could encompass a wide range of frequencies, experimentalists sought a more sensitive and wider-band means of detection. Such a means became available with the development of the laser interferometer, proposed by Forward (14)—and independently by Weiss (15), who also did a detailed noise analysis. This device used the configuration of the Michelson interferometer, described in detail below, to achieve differential sensitivity to the instrument arm length changes caused by an incident gravitational wave. The key idea was that the speed of light accessed in an interferometer, being so much faster than the speed of sound accessed in a bar, enabled the implementation of a much greater measurement pathlength over a cycle of a gravitational wave, which offered correspondingly greater strain sensitivity. The first working laser interferometer, built by Forward (16), was 2 m in arm length and achieved 10^{-16} strain sensitivity in a 1 Hz bandwidth at 1 kHz. Subsequent advanced versions, using improved laser stability, optics, and isolation from background seismic noise, were built at Caltech (17), the University of Glasgow (18), and Garching (19). They were 40, 10, and 30 m in length and achieved strain sensitivities at several hundred hertz in a 100 Hz bandwidth of about 10^{-19} , 10^{-18} , and 10^{-18} , respectively.

After the above prototype demonstrations of high strain sensitivities, funding agencies in the United States and Europe committed to the construction of large, kilometer-scale laser interferometers (described below): LIGO (United States, 4 km), GEO (United Kingdom and Germany, 600 m), and VIRGO (France and Italy, 3 km). These facilities employ the same basic design as the prototypes, but their greater length allows strain sensitivity of order 10^{-22} over a 100 Hz bandwidth, an astrophysically interesting value. All three of these facilities are now undergoing commissioning to reach their full design sensitivity. Advanced detectors of higher sensitivity are being planned in the United States, Europe, and Japan.

The search for gravitational radiation has also secured the interest of the European and American space agencies. An interferometer in space, first proposed by Faller & Bender (20), could be operated at substantially lower frequencies than on the ground. A space-borne detector named LISA (Laser Interferometer Space

Antenna) is now funded for technology development, and launch is scheduled for 2013. LISA will use three spacecraft to form a constellation that will orbit the sun, and will use laser interferometry to sense their relative motion. With a spacecraft separation of 5×10^9 m, LISA will have strain sensitivity at 1 mHz of order 10^{-23} over a one-year integration period (corresponding to a 3×10^{-8} Hz bandwidth).

1.2. Physics of Gravitational Waves

Here we summarize the physics of gravitational radiation in the weak field limit, where considerable insight can be gained. We then use a “back-of-the-envelope” approach to estimating the strength of the radiation and provide references for a complete and rigorous derivation.

1.2.1. GRAVITATIONAL RADIATION In general relativity, space-time is regarded as a four-dimensional manifold with a Lorentzian metric, and gravity is a manifestation of the manifold’s curvature. For our purpose it is sufficient to consider weak gravitational waves as a perturbation on an otherwise Minkowski space-time, i.e., as a perturbation on the space-time of special relativity. Letting $x^\mu = (t, x, y, z)$ denote the time and space coordinates, we can write the proper distance between events x^μ and $x^\mu + dx^\mu$ as

$$ds^2 = g_{\mu\nu} dx^\mu dx^\nu \approx (\eta_{\mu\nu} + h_{\mu\nu}) dx^\mu dx^\nu. \quad 2.$$

Here $\eta_{\mu\nu}$ is the usual Minkowski metric and $h_{\mu\nu}$ represents the linearized gravitational field. Upon linearization, the coordinate invariance of full general relativity is replaced by global Lorentz invariance and local gauge invariance under infinitesimal coordinate transformations $x^\mu \rightarrow x^\mu + \xi^\mu$:

$$h_{\mu\nu} \rightarrow h_{\mu\nu} - \partial_\mu \xi_\nu - \partial_\nu \xi_\mu. \quad 3.$$

The linearized Einstein equations are gauge-invariant, and the gauge freedom can be used to simplify the form of the field equations (21). In the Lorentz family of gauges, $\partial^\mu h_{\mu\nu} = 0$, the Einstein equations (Equation 1) reduce to a simple wave equation that relates the trace-reversed field $\bar{h}_{\mu\nu} = h_{\mu\nu} - \frac{1}{2}\eta_{\mu\nu}h^\alpha_\alpha$ to the stress energy tensor:

$$\left(\frac{\partial^2}{\partial t^2} - \frac{\partial^2}{\partial x^2} - \frac{\partial^2}{\partial y^2} - \frac{\partial^2}{\partial z^2} \right) \bar{h}_{\mu\nu} = 16\pi G_N T_{\mu\nu}. \quad 4.$$

When dealing with gravitational waves, it is convenient to fully gauge-fix the gravitational field so that only physical degrees of freedom remain. A popular choice is the transverse traceless (TT) gauge, in which a plane gravitational wave propagating in the z direction can be written as

$$h_{\mu\nu} = \begin{bmatrix} 0 & 0 & 0 & 0 \\ 0 & h_+ & h_\times & 0 \\ 0 & h_\times & -h_+ & 0 \\ 0 & 0 & 0 & 0 \end{bmatrix}. \quad 5.$$

Here $h_{xx} = h_+$ and $h_{xy} = h_\times$ describe the two polarizations of the gravitational wave. The wave equation (Equation 4) can be solved perturbatively via an expansion in (v/c) where v is the characteristic velocity of masses in the system. When we specialize to TT gauge, the lowest-order contribution yields the so-called quadrupole radiation formula

$$h_{ij}(t, \vec{x}) = \frac{G_N}{c^4} \frac{2}{r} \left[\frac{d^2}{dt^2} Q_{ij} \right]_{\text{ret}}^{\text{TT}}, \quad 6.$$

where

$$Q_{ij}(t) = \int d^3x \left(x_i x_j - \frac{1}{3} x^2 \delta_{ij} \right) \rho(t, \vec{x}) \quad 7.$$

is the trace-free quadrupole moment of the source energy-density distribution and r is the distance to the source. The subscript “ret” in Equation 6 reminds us that the time derivatives should be evaluated at the retarded time $t - r/c$, and the superscript “TT” reminds us to take the transverse projection and subtract the trace. Note that no gravitational wave contribution arises from the source monopole or dipole. The source monopole is, of course, the system’s total mass-energy, which is conserved at linear order. Similarly, the source dipole is related to the system’s center of mass; momentum conservation ensures that a closed system’s center of mass cannot accelerate and, correspondingly, there is no dipole contribution to gravitational waves. As the contribution to the wave amplitude from each ascending multipole term drops in amplitude by a factor c , the absence of the first two terms ensures a very small final amplitude.

The total power radiated by a gravitational wave source can be found by integrating the energy flux through a sphere surrounding the source. Using the quadrupole formula, the luminosity of a source is given by

$$L = \frac{1}{5} \frac{G_N}{c^5} \frac{d^3 Q_{ij}}{dt^3} \frac{d^3 Q^{ij}}{dt^3}. \quad 8.$$

The quadrupole formula and Newtonian gravity can be used to produce simple yet reasonably accurate predictions for the frequency, duration, and strength of gravitational radiation from astrophysical sources.

The effect of a gravitational wave on matter can be described in terms of a tidal acceleration, since what can be measured is not the acceleration itself but its difference across an experiment. The h_+ polarization component of a plane gravitational wave with frequency f propagating in the z direction has the form $h_+(z = 0, t) = h_0 e^{2\pi i f t}$. The tidal acceleration between two points on the x axis separated by $\Delta x = L$ will vary according to

$$\delta \ddot{L} = (2\pi f)^2 L h_0 e^{2\pi i f t}. \quad 9.$$

Thus, the wave imparts a time-varying strain $h = \delta L/L$. According to Equation 5, the plus polarization h_+ will momentarily lengthen distances along the x -axis

while simultaneously shrinking them along the y -axis. The cross polarization h_{\times} has its principal axes rotated by 45° relative to the plus polarization, which is a consequence of the spin-2 nature of the gravitational field.

1.2.2. BACK-OF-THE-ENVELOPE ESTIMATES Here we follow the approach of Schutz (22) and use Newtonian gravity, supplemented by the Einstein quadrupole formula (6), to estimate the frequency and strength of gravitational waves from astrophysical bodies.

Self-gravitating systems have a natural dynamical frequency associated with the mean mass density ρ of the system:

$$f_{\text{dyn}} = \frac{1}{2\pi} (\pi G_N \rho)^{1/2} \sim \left(\frac{G_N M}{16\pi R^3} \right)^{1/2}. \quad 10.$$

Here M is the mass of the system and R is its characteristic size. For example, if the object in question is a binary star system, R would be the size of the semimajor axis and Equation 10 would be a statement of Kepler's law. The time variation of the quadrupole moment can be related to f_{dyn} by

$$|\ddot{Q}_{ij}| < \frac{d^2}{dt^2} \int \rho x^2 d^3x \sim (2\pi f_{\text{dyn}})^2 MR^2. \quad 11.$$

This expression is only an upper limit, as we have ignored the projection and trace removal. Moreover, the quadrupolar nature of the waves implies that only the nonspherical component of the mass distribution should be considered in Equation 11. For highly nonspherical mass distributions, such as a binary star system, it is enough to reduce the estimate in Equation 11 by a factor of two. Combining Equations 10 and 11 with the quadrupole formula (Equation 6) yields the estimate

$$h \sim 2 \left(\frac{G_N M}{Rc^2} \right) \left(\frac{G_N M}{rc^2} \right) \quad 12.$$

for the amplitude of a gravitational wave. The first term in brackets is just the internal gravitational potential of the system, while the second term in brackets, where r is the distance to the source, is the gravitational potential of the system at the observer's location. The combination $R_G = G_N M/c^2$ is the gravitational radius of the system (~ 1.5 km for the sun), and R must be greater than R_G or else the entire system is inside a black hole. Because the first factor in Equation 12 cannot exceed unity, and because the typical distance to a gravitational wave source greatly exceeds 1 km, it is clear that even the brightest gravitational wave sources will have extremely small amplitudes.

The gravitational wave frequency f is typically equal to twice the dynamical frequency f_{dyn} because quadrupole distributions are reflection-symmetric. The duration of a source can be estimated by comparing the luminosity to the gravitational potential energy. The time derivatives in Equation 8 bring down two additional factors of $2\pi f_{\text{dyn}}$, leading to a luminosity estimate of

$$L \sim \frac{\pi c^5}{G_N} \left(\frac{G_N M}{R c^2} \right)^5. \quad 13.$$

The factor $\pi c^5/G_N = 1.1 \times 10^{53}$ W sets the upper limit for the luminosity of any gravitational wave source, since the second factor, $(R_G/R)^5$, cannot exceed unity. The gravitational wave frequency increases on a characteristic time scale, τ_{gw} , which can be estimated by calculating the time for the system to radiate half its gravitational potential energy:

$$\tau_{\text{gw}} = \frac{1}{L} \frac{G_N M^2}{2R} = \frac{R}{2\pi c} \left(\frac{G_N M}{R c^2} \right)^{-3}. \quad 14.$$

The factor R/c is the light crossing time for the system, and the factor $(R/R_G)^3$ is a measure of the compactness of the system. As a radiating system becomes more compact, the amplitude of the wave increases, as does its frequency and the rate of change of its frequency. These increases result in a characteristic “chirping” signal. It is interesting to note that the observation of h , f , and τ_{gw} allows us to derive the distance r to the source, as well as the source mass M and size R . Thus, a system decaying through the emission of gravitational radiation provides a standard candle for distance measurement (23). (Gravitational wave observations are unable to measure the redshift of a source, so an optical counterpart is needed to probe the redshift-distance relation.)

It is instructive to apply our back-of-the-envelope estimates to promising sources of gravitational waves, such as a binary star system consisting of two 1.4 solar mass neutron stars separated by 90 km at a distance of 15 Mpc (i.e., the approximate distance to the center of the Virgo Cluster of galaxies). The evolution of a binary system driven by gravitational wave emission is divided into three main phases: inspiral, merger, and ringdown. The inspiral phase sees the orbit shrink as the gravitational waves carry off energy and angular momentum, eventually driving the two components of the binary to merge. The end product of the merger is either a highly distorted star or a black hole that relaxes by emitting gravitational waves in the ringdown phase. We find that the amplitude, frequency, and duration of the source are given by

$$h \approx 10^{-21} \left(\frac{15 \text{ Mpc}}{r} \right) \left(\frac{M}{2.8 M_\odot} \right)^2 \left(\frac{90 \text{ km}}{R} \right), \quad 15.$$

$$f = \left(\frac{M}{2.8 M_\odot} \right)^{1/2} \left(\frac{90 \text{ km}}{R} \right)^{3/2} 100 \text{ Hz}, \quad 16.$$

$$\tau_{\text{gw}} = \left(\frac{R}{90 \text{ km}} \right)^4 \left(\frac{2.8 M_\odot}{M} \right)^3 0.5 \text{ s}. \quad 17.$$

A set of numerical examples is shown in Table 1. The first example gives the strain amplitude of a supernova burst from a stellar collapse to a neutron star, where we have assumed 0.1% of the collapse energy is nonspherical. In this case we use

TABLE 1 Strain amplitude estimates for supernova and binary inspirals

Source	H	f (Hz)	M (M_{\odot})	R (km)	r (Mpc)
Supernova	10^{-21}	—	1.4	—	10
NS-NS Inspirals	10^{-21}	100	2.8	90	15
MBH-MBH Inspirals	10^{-16}	10^{-4}	10^7	10	1000

Equation 12 and assign the first factor (expressing the internal potential) a value of ~ 0.2 for a neutron star. The second example gives the strain amplitude and frequency (Equations 15 and 16) from the inspiral of a neutron star binary system, sought by the ground-based gravitational wave detectors. In this case all the source energy is nonspherical. The third case describes a supermassive black hole binary inspiral, within one year of its merger, which will be sought by a space-based detector. These sources and detectors are described in the following sections.

The calculations described above are accurate to within an order of magnitude or better of a full relativistic treatment, which is beyond the scope of this article. For a comprehensive treatment, including the subject of strong-field gravity, the reader is referred to References 21, 24, and 25.

1.3. Basic Analysis Concepts

We present here a number of basic concepts related to the detection, analysis, and interpretation of gravitational wave signals and noise, which will be used throughout the article.

The output of a gravitational wave detector is a time series $s(t)$ that includes instrument noise $n(t)$ and the response to the gravitational wave signal $h(t)$:

$$s(t) = F^+(t)h_+(t) + F^\times(t)h_\times(t) + n(t). \quad 18.$$

The instrument response is a convolution of the antenna patterns F^+ , F^\times with the two gravitational wave polarizations h_+ , h_\times . The antenna patterns depend on the frequency and sky location of the source; for wavelengths that are large compared to the detector, the antenna patterns are simple quadrupoles.

The information contained in the time series is usually represented in the Fourier domain as a strain amplitude spectral density, $h(f)$. This quantity is defined in terms of the power spectral density $S_s(f) = \tilde{s}^*(f)\tilde{s}(f)$ of the Fourier transform of the time series

$$\tilde{s}(f) = \int_{-\infty}^{\infty} e^{-2\pi ift} s(t) dt. \quad 19.$$

The strain amplitude spectral density is then defined as $h(f) = \sqrt{S_s(f)}$. In an analogous manner, we can describe the noise power spectral density $S_n(f)$ and the signal power spectral density $S_h(f)$. Another important quantity is the characteristic

strain, $h_c(f)$, which is defined as

$$h_c(f) = \sqrt{f S_s(f)}. \quad 20.$$

The characteristic strain is essentially the rms signal in a frequency interval of width $\Delta f = f$ centered at frequency f . Most plots showing instrument sensitivity curves and source strengths utilize one of these quantities.

Finally, we briefly discuss the description of gravitational wave sources that are not discretely resolvable, known as stochastic background sources. Stochastic backgrounds of gravitational waves can be produced by processes in the early universe and by the superposition of the signals from many independent sources. The techniques for calculating these signals, and the language for describing them, differ from those used to treat isolated sources. The gravitational waves from sources such as binary neutron stars encode information about the coherent, bulk motion of the system. In contrast, the phase incoherence of the stochastic background forces us to work with quantities such as energy density. The energy density in a gravitational wave is given by

$$\rho_{\text{gw}} = \frac{1}{32\pi G_N} \langle \tilde{h}^2 \rangle. \quad 21.$$

Here the brackets denote a spatial average over several wavelengths. For a stochastic background, the spatial averaging is equivalent to taking an ensemble average of the fields (also denoted by angle brackets). The ensemble average of the Fourier amplitudes of an unpolarized, Gaussian, stationary background can be described in terms of the spectral density $S_h(f)$:

$$\langle \tilde{h}^*(f) \tilde{h}(f') \rangle = \delta(f - f') S_h(f). \quad 22.$$

Combining Equations 19, 21, and 22, we have

$$\rho_{\text{gw}} = \frac{\pi}{2G_N} \int_0^\infty df f^2 S_h(f). \quad 23.$$

It is standard practice to quote the strength of a stochastic background in terms of the energy density per logarithmic frequency interval, $d\rho_{\text{gw}}/d \ln f$, scaled by the energy density needed to close the universe:

$$\Omega_{\text{gw}}(f) = \frac{1}{\rho_{\text{crit}}} \frac{d\rho_{\text{gw}}}{d \ln f} = \frac{4\pi^2}{3H_0^2} f^3 S_h(f). \quad 24.$$

Here H_0 is the Hubble constant and ρ_{crit} is the critical density. The total energy density in gravitational waves, in units of the critical density, is then $\Omega_{\text{gw}} = \int \Omega_{\text{gw}}(f) d \ln f$. [To avoid the ambiguity associated with the different values of H_0 quoted in the literature, we define the factor $h_{100} = H_0/H_{100}$ where $H_{100} = 100 \text{ km}/(\text{s Mpc})$, and work with the quantity $\Omega_{\text{gw}} h_{100}^2$, which is independent of the Hubble expansion rate.] Standard inflationary cosmological models predict a scale-invariant spectrum with $\Omega_{\text{gw}}(f) = \text{const.}$ over many decades in frequency.

The direct experimental bounds on $\Omega_{\text{gw}}(f)$ described in later sections are for a scale-invariant spectrum.

2. SOURCES: MODELS, STRENGTHS, AND RATES

In this section, we review our present understanding of gravitational wave sources, covering 22 decades of frequency from 10^{-18} to 10^4 Hz, and discuss some insights that may be gained by their detection.

2.1. Source Modeling

Astrophysical sources of gravitational waves are expected to produce a range of signals, including bursts, chirps, sinusoids, and stochastic backgrounds. Considerable effort has gone into anticipating the types of astrophysical systems that will produce detectable gravitational wave emissions, and into accurately modeling the waveforms these systems produce. Precision tests of strong-field general relativity require these waveforms for comparison with experiment; also, the identification of a gravitational wave signal in a noisy background is significantly aided by knowledge of the precise signal waveform (see discussion in Section 4).

However, calculation of the waveforms is difficult. Beyond understanding the physical processes in core collapse, matter accretion, and other relevant problems, solving the Einstein tensor equations (Equation 1) involves handling 10 coupled, nonlinear partial differential equations subject to dynamically evolving boundary conditions. The calculations are, of course, also complicated by the presence of singularities. The coordinate system and gauge may be freely chosen, but in most cases the appropriate choice is not at all obvious. Two examples may illustrate the current issues in the modeling of gravitational waveforms.

An important computational problem is the case of stellar mass capture by a massive black hole. To date, no one has managed to calculate the highly eccentric orbit necessary to generate a matched filter for its detection in a noisy background. The extreme mass ratio of this source allows perturbative techniques to be brought to bear, with some success (26). However, a serious difficulty is the large parameter space needed to specify a particular orbit and the propensity of certain orbits to explore vast regions of their available phase space. A complete calculation requires a detailed understanding of, and computational facility with, radiation reaction forces in general relativity. Such mastery does not exist today, though much progress has been made on this problem in recent years. A complete algorithm for calculating the waveforms has been proposed but not yet implemented (27).

A second problem is the inspiral of an equal-mass binary black hole (BH-BH) system. The BH-BH merger signal is particularly difficult to calculate: No approximations apply in this case, and a comparison of observation with theory will become possible only when we can pose relevant initial data and numerically simulate the Einstein equations. These simulations, known as numerical relativity (28), encounter serious difficulties. First, regardless of the form of the equations used or the structure of the mesh on which the equations are evaluated, all current

simulations encounter disabling numerical instabilities. Second, the correct initial conditions for the transition from a computationally tractable to highly nonlinear regime are not yet well understood. Current research in numerical relativity involves both these topics, including adaptive mesh refinement techniques (29).

On the other hand, there are many sources for which the waveform modeling is well understood. An example is the early inspiral phase of binary systems of neutron stars, white dwarfs, or black holes. The techniques are similar to those described in Section 1.2 and involve a weak-field, slow-motion expansion of the Einstein equations. This so-called post-Newtonian expansion has now been extended to order $(v/c)^6$ (see Reference 30).

The gravitational wave stochastic background spectrum from the early universe is another well-modeled source. For example, slow-roll inflation predicts an essentially scale-free primordial spectrum with $\Omega_{\text{gw}} \sim 10^{-15}$ or less, which extends over the entire gravitational wave spectrum discussed in the following sections. Standard sensitivity plots for gravitational wave detectors show the square root of the spectral power as a function of frequency (or other closely related quantities), so a scale-invariant stochastic background will appear with a slope of $f^{-3/2}$ in these plots.

2.2. Extremely Low Frequency (10^{-18} Hz to 10^{-15} Hz)

The principal expected source for gravitational radiation in the 10^{-18} Hz to 10^{-15} Hz frequency range is primordial gravitational fluctuations amplified by the inflation of the universe. Inflation predicts that quantum fluctuations in the space-time metric would give rise to a gravitational wave background, with the amplitude of the background fixed by the vacuum energy density during inflation (31). With recent measurements of the cosmic microwave background (CMB) supporting several fundamental predictions of inflation, such as the flatness of the universe and the presence of coherent oscillations in the primordial plasma, observation of the gravitational wave background presents an important new test of the theory.

The mechanism for detecting these waves in the extremely low frequency band is via their imprint on the polarization of the CMB radiation. Gravitational waves will produce a curl component of the polarization, whereas density perturbations will not (32). (Gravitational lensing of the CMB due to large-scale structure along the line of sight can cause a polarization curl component at the surface of last scatter even in the absence of gravitational waves, but this effect can be mapped with high-order CMB correlations.) Detection of a curl component in the CMB would identify a vacuum energy scale during inflation of 10^{15-16} GeV and would thus associate inflation with the characteristic era of grand unification.

2.3. Very Low Frequency (10^{-9} Hz to 10^{-7} Hz)

Sources expected in the very low frequency band are processes in the very early universe, including the big bang, and topological defects such as domain walls and cosmic strings. Another expected source is first-order phase transitions in the

early universe, corresponding to symmetry breaking of fundamental interactions; the collision of nucleated vacuum bubbles forming around the potential barrier associated with the phase transition will lead to gravitational radiation in this frequency range (33). The inspiral of supermassive black holes (mass greater than 10^{10} solar masses) can also lead to waves with frequencies in this range.

The wavelengths of these sources are sufficiently long that they cannot be studied with either ground- or space-based detectors. However, their effect on the arrival time of pulsar signals may be observable with pulsar timing arrays, described below.

2.4. Low Frequency (10^{-4} Hz to 1 Hz)

This section describes sources whose strength and number are high enough to make them candidates for detection by LISA, the space-based detector mentioned above and described in Section 3.

2.4.1. GALACTIC BINARIES Approximately two out of every three stellar systems are multiple-star systems. In a significant fraction of stellar binaries, both members undergo supernova explosion during their evolution, resulting in the formation of compact binary systems composed of neutron stars (NS) or black holes (BH). In other cases, both members evolve through a red giant phase before forming a white dwarf (WD) binary. In a smaller fraction of the compact binaries, the members may be sufficiently close to emit gravitational radiation at frequencies above 10^{-4} Hz.

The population estimates used to predict LISA detection of the binary systems have considerable uncertainty due to their sensitive dependence on assumptions about mass loss during the evolution of giant stars; nevertheless, the numbers are expected to be large. About a dozen known optical systems will be observed, including a WD-WD binary system about 100 pc from the earth (WD 09570666) and a low-mass x-ray binary that consists of a $1.4 M_{\odot}$ neutron star accreting mass from a $0.1 M_{\odot}$ orbiting star ~ 8 kpc from the earth (4U1820-30).

The number of compact binaries in our galaxy with orbital periods in the LISA band is of order 10^8 , most of them close white dwarf binaries (CWDBs). CWDB orbits decay because of gravitational wave emission, which is greater at higher orbital frequencies, leaving most systems at low orbital frequency. At frequencies below a few millihertz, there are so many CWDB systems that only the brightest systems can be individually resolved over the LISA mission lifetime of several years. Thus, at frequencies below several millihertz, the gravitational wave signals from the many CWDBs will appear to LISA as a confusion-limited background owing to the incoherent superposition of the gravitational waves from the many CWDB systems (34). Above a few millihertz, the number of CWDB systems drops appreciably; there are about 3000 above 3 mHz, and the majority of these systems will be individually resolvable. For ~ 1000 of the highest frequency binaries, measurement of the source frequency and its rate of change will allow its distance to be calculated. The pointing accuracy of LISA ($\sim 0.3 \rightarrow 3^{\circ}$ for these systems) will

then allow the construction of a three-dimensional CWDB map of the galaxy. Up to 10% of the CWDB systems observed by LISA will be seen by optical follow-ups (35), enabling interesting cross comparisons and tests of fundamental physics. For example, by comparing the arrival times of the gravitational and electromagnetic signals, it will be possible to place improved bounds on the mass of the graviton (36).

NS-NS and NS-BH binaries also populate our galaxy in substantial numbers, $\sim 10^6$. They will be detectable by LISA, although the rate is highly uncertain.

2.4.2. MASSIVE BLACK HOLE BINARY MERGER Observational evidence for massive black holes (MBHs) with mass between 10^4 and $10^9 M_\odot$ is strong, including clear evidence, from near-IR astrometric imaging, for a $3 \times 10^6 M_\odot$ black hole at the center of our galaxy (37). MBHs have also been identified in many closely studied, nearby galaxies; thus, their total number throughout the universe is likely to be large. The mechanism for MBH formation is uncertain. One proposal is that a massive star forms in the potential well of a young galaxy and collapses into a MBH (38). Another is that collisions in dense star clusters in a galactic nucleus build up seed MBHs to a mass sufficiently high ($\sim 10^3 M_\odot$) that growth can proceed rapidly through gas absorption and tidal disruption of stars (39).

An MBH binary coalescence is believed to occur during the merger of galaxies. In the standard picture of galactic structure formation, protogalaxies merge to form larger galaxies. Dynamical friction then brings the MBHs to the common center where the coalescence takes place (40). Thus, observation of the merger can provide insight into the early formation of galaxies. Black hole mergers are also the ultimate manifestation of nonlinear gravity, and the signal that arises from this stage of the MBH-MBH binary coalescence provides an opportunity to test gravity in its most strong-field, dynamical regime. The signal that arises at the end of the coalescence, as the final, single black hole rings down into its final, stationary state, is also very revealing. The ringdown radiation has a characteristic spectrum that depends only on the black hole's spin and angular momentum and can be calculated via perturbation theory (41). This result derives from the so-called "no-hair" theorem, which states that astrophysical black holes are characterized only by their mass and angular momentum. The observation of a spectrum inconsistent with that predicted by general relativity for compact, 10^4 – 10^7 solar mass objects will signal new physics; either general relativity does not correctly describe gravity or there are previously unknown matter fields that can support compact objects in this mass range. Alternatively, if the spectrum is consistent with a general relativistic black hole, it will reveal the black hole's mass and spin (42).

The detectability of MBH mergers depends on the time from coalescence, as well as mass and distance. The signal-to-noise ratio for these events is such that LISA can see a coalescence of two $10^4 M_\odot$ black holes 100 years before the merger at 1000 Mpc and anywhere in the universe during the last year before the coalescence. The event rate is very uncertain; estimates of MBH coalescences out to $z = 1$ vary from 0.1 to 100 per year (43), where z is the redshift.

2.4.3. MBH CAPTURE OF COMPACT OBJECT Massive or supermassive black holes at the center of clusters or galaxies “capture” stellar-mass white dwarfs, neutron stars, or black holes. The many-body dynamics of the cluster “injects” stellar-mass compact objects into (elliptical) orbits about the more massive black hole. Gravitational wave emission causes the orbits to decay, until the stellar-mass object falls through the horizon of the MBH. Much of the radiation in the several years immediately preceding the coalescence will be observable by LISA; the detailed phase evolution of the gravitational waves will reflect the orbital evolution of the stellar-mass compact binary, which in turn is determined by the local geometry of the space-time about the MBH. Thus, a high-precision map of the strong-field space-time about a black hole can be obtained from observations of capture systems (44) and compared to predictions of general relativity, allowing it to be tested in the strongest field regimes.

The radiation generated from the inspiral orbit will map with high accuracy the Kerr geometry of the MBH, and will allow a high-precision test of the fundamental “no-hair” theorem of general relativity: The black hole’s properties are completely determined by its mass and spin. Information about the MBH mass, spin, and position will be obtained (45).

Signal-to-noise ratios of 10–100 are possible for observations made in the LISA detector if the exact time dependence of the signal is known in advance and optimal filtering techniques, which require the use of signal templates, can be used (see Section 4.1). Generating a sufficiently large bank of templates will be challenging given the large parameter space that has to be explored. A further concern is that capture sources may be so abundant that we will be unable to resolve individual capture systems, leading to a confusion background similar to that of the galactic binaries discussed above.

Figure 1 shows two segments of a waveform from the inspiral of a black hole of $1 M_{\odot}$ into a $10^6 M_{\odot}$ hole. Both early and late times in the inspiral are shown. A notable feature is the low frequency modulation at late times caused by inertial frame dragging from the black hole spin (46).

The rate for this event is likely to be substantial because a significant fraction of galaxies contain MBHs, and LISA can observe inspirals of compact objects as small as $1 M_{\odot}$ into an MBH out to 1 Gpc. Present estimates are $\sim 100/\text{y}$ for $\sim 10 M_{\odot}$ black holes out to 6 Gpc (47).

2.4.4. COLLAPSE OF SUPERMASSIVE STAR The instability and collapse of a supermassive star may be involved in the formation of supermassive black holes, with mass greater than $10^6 M_{\odot}$, known to exist in the centers of many, if not most, galaxies. The collapse of the supermassive star may lead to substantial gravitational wave emission, depending on the collapse asymmetry. A possible mechanism for a highly asymmetrical collapse is the development of a dynamical bar-mode instability as the supermassive star cools. This may be likely if viscosity and magnetic fields are insufficient to keep the star rotating uniformly during cooling. Given enough energy and a long enough lifetime of the bar mode, a significant fraction

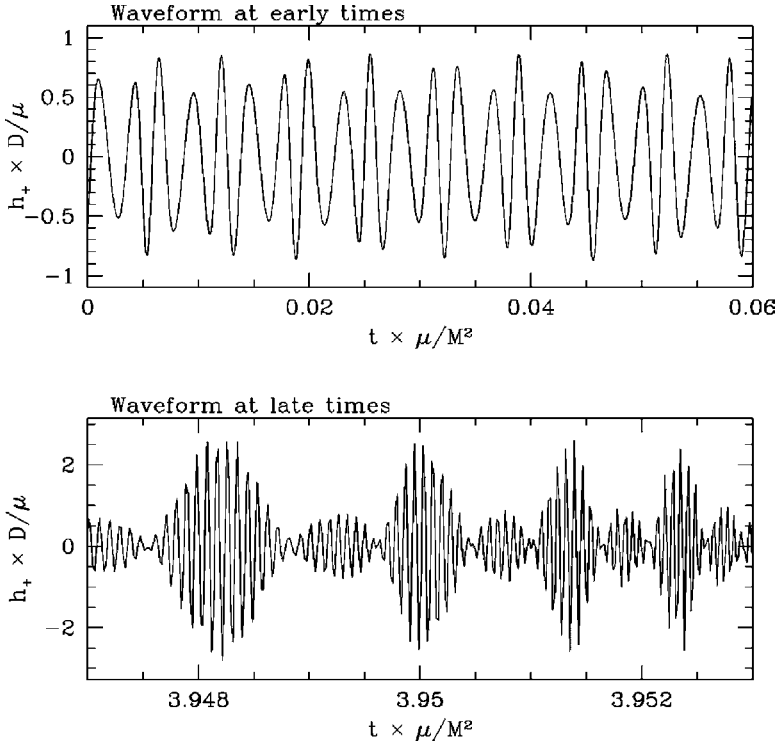


Figure 1 Stellar mass capture by a massive black hole. The waveform at late times shows frequency modulation from frame dragging by the black hole's spin. (From Reference 46 with permission.)

of the star's rest energy could be lost as gravitational radiation. For example, a $10^6 M_\odot$ supermassive star at 1 Gpc could produce a detectable source for LISA in a year-long 0.3 mHz burst by radiating 0.1% of its mass (48). Significant work remains to be done on the modeling of this process.

2.4.5. STOCHASTIC BACKGROUND The anticipated stochastic background in the low frequency range is a combination of primordial and astrophysical sources, which combine to produce a diffuse background that can only be described statistically.

The astrophysical contribution to the background will be from a combination of binary systems with main sequence stars, white dwarfs, neutron stars, or stellar mass black hole components. The astrophysical signal from binaries will dominate at frequencies below a few millihertz and is expected to limit the sensitivity to the primordial signal to $\Omega_{\text{gw}} \sim 10^{-11}$. The primordial contribution to the stochastic background depends on the source. Amplification of quantum fluctuations by inflation, for example, is predicted to contribute at a level of $\Omega_{\text{gw}} < 10^{-15}$, which is

too weak compared to the astrophysical confusion background at these frequencies (49). Nevertheless, other early-universe physics may be observable. For example, gravitational waves from phase transitions are peaked around a frequency that depends on the temperature T of the phase transition:

$$f_{\text{peak}} \sim 10^{-3} \text{ Hz} \left(\frac{T}{\text{TeV}} \right). \quad 25.$$

If the electroweak phase transition, which occurs at a temperature of 100 GeV, is strongly first-order, it could lead to a measurable signal at 10^{-4} Hz. Another source for a stochastic background is the superposition of gravitational waves produced by excited cosmic strings (50). This spectrum, constrained by millisecond pulsar observations (see below), suggests $\Omega_{\text{gw}} < 10^{-8}$. Other more exotic possibilities include cosmic strings and brane worlds [LISA can probe extra dimensions at a scale of $1\text{--}10^{-6}$ mm (51)]. Finally, big bang nucleosynthesis provides limits on the amplitude of this background; gravitational waves with wavelengths shorter than the horizon size at the time of nucleosynthesis affect the expansion rate and thus the universal abundance of light elements (52), leading to the bound $\Omega_{\text{gw}}(f > 10^{-9} \text{ Hz}) < 10^{-5}$.

Several low frequency sources are shown in Figure 2. The LISA detector rms sensitivity curve is plotted as a characteristic strain, $h_n = \sqrt{S_n(f)\Delta f/R(f)}$, with a bandwidth Δf equal to the frequency f , and the function $R(f)$ which takes

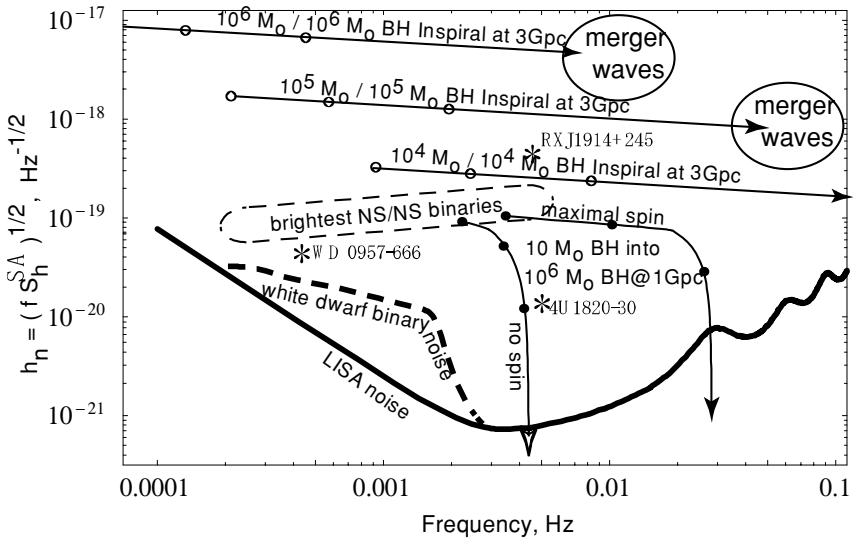


Figure 2 Signal strength of several gravitational wave sources sought by the space-based detector LISA. Also shown is the LISA rms noise over a bandwidth equal to the frequency. The dots on the arrow curves denote 1 year, 1 month, and 1 day before the binary mergers. (From Reference 53 with permission.)

into account the averaging of the detector sensitivity over all sky locations and polarizations (53). (The LISA sensitivity is described in detail in Section 3.) The characteristic source strains, $h_c = \sqrt{S_h(f)\Delta f}$, in Figure 2 have been multiplied by a factor equal to the square root of the number of frequency bins in the bandwidth, $\sqrt{\Delta f T_{\text{obs}}}$, to represent the improvements in the signal-to-noise ratio that can be achieved by coherent matched filtering. Without this factor, many of the signals in Figure 2 would be at or below the sensitivity curve.

2.5. High Frequency (10^1 Hz to 10^4 Hz)

Sources in the high frequency range will be sought by ground-based gravitational wave observatories, described in Section 3.

2.5.1. COMPACT BINARY COALESCENCE These sources include the final hours of the coalescence of binary systems of neutron stars and black holes of mass less than $100 M_\odot$ (Masses greater than this develop signal power outside the bandwidth of ground-based detector systems.) The coalescence involves three phases: the “inspiral,” when the orbit evolves adiabatically owing to emission of gravitational radiation; the “merger,” when the binary components collide; and the “ringdown,” when the final merged system settles into an equilibrium state by radiating away its distortions.

During the inspiral, both the amplitude and frequency of the emitted gravitational wave rise, producing a chirp that sweeps across the detection band (see Figure 3). The signal amplitude from a compact binary inspiral is well approximated by a post-Newtonian analysis.

During the final 15 min of a NS-NS inspiral, the nearly periodic signal evolves from 10 Hz to ~ 1 KHz, when the neutron stars merge. A NS-NS inspiral may be observed in the initial LIGO (using three interferometers) to a range of 20 Mpc and in the advanced LIGO to 350 Mpc. For BH-BH inspirals, the larger masses result in stronger signals and yield ranges of 100 and 1000 Mpc for the initial and advanced detectors, respectively.

The rate for the stellar-mass compact binary coalescence has been estimated on the basis of five observed binary pulsar systems in our galaxy that will coalesce in less than a Hubble time (i.e., the present age of the universe). Binary pulsar systems are one component of a distribution of stellar-mass neutron star and black hole binary systems; the distribution is estimated by modeling the evolution of its massive star progenitors. By taking into account the fraction of the entire galactic population that is observable to us as a binary pulsar system and the number of binary pulsar systems actually observed, we can estimate the galactic coalescence rate. From that rate, the rate of coalescence events detectable by, e.g., the LIGO detectors can be estimated. This leads to an event rate for NS-NS coalescences of 10^{-2} to 1 per year in the initial LIGO detectors (54). The BH-NS detection rate is expected to be approximately half the NS-NS rate, whereas the BH-BH detection rate will be ~ 10 times larger than the NS-NS rate (55). The large uncertainties in

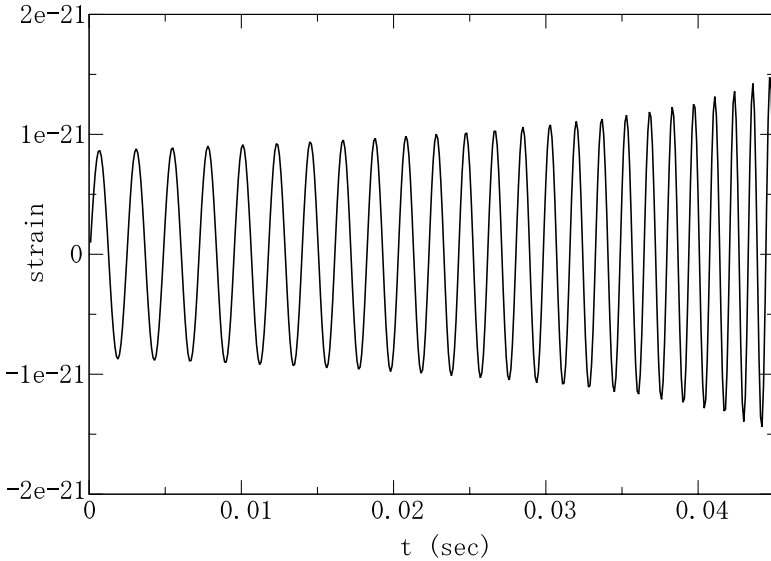


Figure 3 Chirp signal from inspiraling neutron star binary at a distance of 10 Mpc. At the end of the waveform, the neutron stars are separated by ~ 30 km.

the rate estimates are due to (a) the small number of observed galactic binary pulsar systems; (b) uncertainties in the observational selection effects, which determine the fraction of the total population of binary pulsar systems that we expect to observe; and (c) uncertainties in the binary synthesis and evolution models that predict the branching ratio of progenitor systems into NS-NS, NS-BH, or BH-BH.

The gravitational wave signal associated with compact binary coalescence depends principally on the component masses and orbital eccentricity. Gravitational radiation tends to circularize orbits, and for these systems the eccentricity will be effectively zero. For systems consisting of, for example, a 1.4 solar-mass neutron star on a 10 solar-mass black hole, spin-orbit coupling can lead to precession of the orbital plane, which will leave an impression on the signal (56). From the observed inspiral signal, many of the binary systems properties can thus be determined (57).

The transition from inspiral to merger depends on the mass and mass-radius relationship for the binary components. For black holes the relationship is trivial; for neutron stars the mass-radius relationship depends on the unknown equation of state of cold, bulk nuclear matter at supernuclear densities. The inspiral-merger transition can in principle be identified in the coalescence waveform, providing information of the supernuclear equation of state (58).

The signal from this stage of the BH-BH binary coalescence provides another opportunity to test gravity in the strong-field, dynamical regime. As described in the above discussion of MBH mergers, observation of the merger (and ringdown) signals provides a precision test of general relativity and a definitive test that the

remnant is, in fact, a black hole, although the merger is particularly difficult to calculate (41).

The advanced LIGO detector, described below, will have a sensitivity at least 10 times higher than the initial LIGO. With a detection range proportional to sensitivity, and the volume of space surveyed proportional to the range cubed, rates for the advanced LIGO detector could be 1000 times higher, which would result in a high probability of many compact binary coalescence detections per year.

2.5.2. SPINNING NEUTRON STAR The degree to which a spinning neutron star emits gravitational radiation is characterized by its ellipticity (ε_e), which is the fractional deviation from sphericity of the star. From Equation 6 we arrive at the gravitational wave amplitude

$$h \sim \frac{G I f^2 \varepsilon_e}{c^2 r}, \quad 26.$$

where I is the star's moment of inertia, f is the wave frequency (twice the star rotation frequency), and r is the distance to the star. A number of channels have been proposed that provide neutron star ellipticity, including crustal irregularities, which may develop through the process of accretion and associated crustal fracturing (59). A buried magnetic field could force the neutron star into a prolate shape (60); ellipticities of order 10^{-7} are possible for plausible values of the magnetic field, $\sim 10^{13-15}$ G. An oblate axisymmetric crustal shape may also be assumed when a newborn neutron star attains its final state.

An upper limit for ε_e , based on theoretical predictions of crustal shear moduli and breaking strengths, is a range of 10^{-4} to 10^{-6} . These inputs suggest values for galactic sources of $h \sim 10^{-24}$ or less; detection will therefore require averaging the signal over many wave periods. A complication in the data analysis is that the earth's rotational and orbital motion will modulate the source frequency, requiring correction of the modulation as a function of the source sky position. This will be possible for known pulsars, whose position and frequency have been identified in advance. However, searching for periodic waves from unknown sources will require significant investments of computational resources, as well as the implementation of hierarchical search algorithms.

Upper limits for ε_e have also been set for known pulsars by observation of the spindown, assuming that the only mechanism for the energy loss is the emission of gravitational waves. For millisecond pulsars this leads to $\varepsilon_e < 10^{-7}$.

2.5.3. STELLAR COLLAPSE, SUPERNOVAE, AND GAMMA-RAY BURSTS The collapse of a massive star, after gravitation overwhelms the pressure sustained through nuclear burning, results in a supernova explosion and the remnant of a neutron star or black hole. The core collapse, if it is sufficiently asymmetric, has sufficient mass dynamics to be a source of gravitational waves; however, the physics of the process from collapse to compact object formation is not well understood. Observation of such an event in our galaxy, coupled with neutrino and optical signals, could

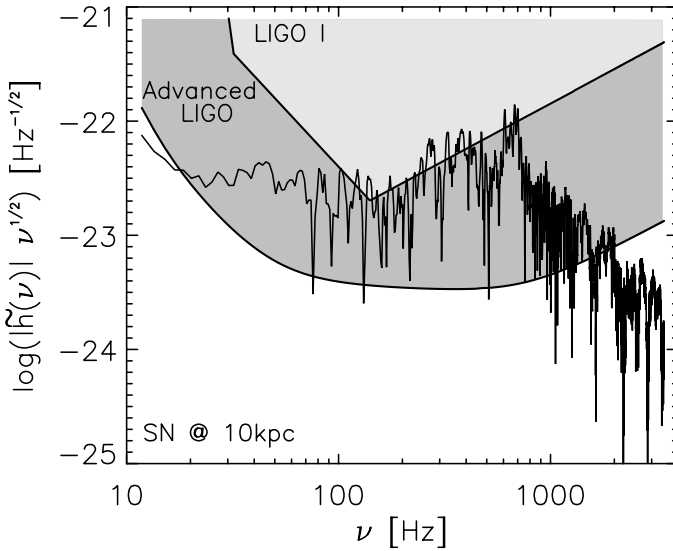


Figure 4 Gravitational wave strain spectrum from stellar collapse. (From Reference 61 with permission.)

do much to enhance our understanding of the collapse process, although such events are rare (several per century per galaxy.) Figure 4 shows the expected strain spectrum for a core collapse supernova at a distance of 10 kpc (61). Recent calculations find that the dominant contribution to the gravitational wave signal is neutrino-driven convection in the postshock region.

A type II supernova explosion leads to the formation of a neutron star or black hole. Out to a distance of 10 Mpc, a supernova occurs about once per year. One suggested mechanism for wave generation is a fast-spinning proto-neutron star that deforms to a bar-shaped object tumbling end over end. At this distance, the entire star's core would need to evolve into a rotating bar for the gravitational wave signal to be observable (62). Thus, a detection is more likely within our galaxy, although these occur at a substantially reduced rate (about 1 every 30 years).

Gamma-ray bursts (GRBs) are flashes of gamma rays that last from <1 s to hundreds of seconds and release energy at $\sim 10^{51-54}$ erg/s, the highest luminosity of any known astrophysical source (63). GRBs fall into two classes, short (<2 s) and long (>2 s). The present leading candidate mechanism for long GRBs is a collapsar (64); for short GRBs there is no consensus model, but they may be associated with compact object coalescence (65). The result in both cases is the violent formation of a black hole; however, the associated gravitational wave emission is very uncertain. Estimates for signal strength from collapsars range from 10^{-22} to 10^{-25} at 10 Mpc, depending on the specific model (66, 67). If the burst is due to a NS-BH inspiral, advanced LIGO could see about 30 per year. Individual GRBs that occur at cosmological distances associated with the short burst category are unlikely to be seen by gravitational wave detectors. However, by correlating

detector outputs immediately before a burst and at other times, it will still be possible to observe a statistical association between gravitational waves and GRBs. Such an observation would allow a test of the general knowledge of these sources, including the time delay between the gravitational wave and the GRB (68). The launch of SWIFT in 2004, a two-year NASA mission designed for the detailed study of GRBs and their afterglows at an expected rate of about one per day, will provide an electromagnetic trigger signal for the gravitational wave search (69).

2.5.4. STOCHASTIC BACKGROUND Processes in the early universe will contribute to the high-frequency gravitational wave stochastic background. The bound $\Omega_{gw}(f > 10^{-9} \text{ Hz}) < 10^{-5}$ (from nucleosynthesis) is close to the sensitivity of the initial LIGO detector in the band from 100 to 1000 Hz.

A variety of mechanisms have been proposed that may have produced gravitational waves in the early universe ($t \sim 10^{-25}$ s), resulting in waves redshifted into the advanced LIGO detection band, which will have a detection sensitivity of $\Omega \sim 10^{-10}$ over a one-year integration time. Inflationary models predict parametric amplification of fluctuations created in the Plank era; some modifications to standard inflation predict a signal detectable by LIGO (70). Also, efforts to develop a model of the very early universe that incorporates superstring theory predict a high-frequency rise in the gravitational wave spectrum (71), which could be detectable by LIGO.

Other possible inputs to the stochastic wave background include first-order phase transition in the quantum field producing waves; excitations of scalar fields arising in string theories; and coherent excitations of our universe, regarded as a “brane” in a higher-dimensional universe (72). The early-universe region of time discussed here, 10^{-25} s, will be explored for the first time through gravitational wave emission in the ground-based detectors.

Figure 5 summarizes a number of the above sources, along with the amplitude noise spectral densities (see Section 1.3) of the initial and advanced LIGO detectors, described in Section 3. The signals shown in Figure 5, like those in Figure 2, are not the raw strain spectral densities. Rather, the signal levels are meant to represent the signal-to-noise ratios that can be achieved using optimal data-analysis techniques (53).

3. MEASUREMENT TECHNIQUES

In this section, we describe the techniques and facilities that have been developed to achieve the extremely high displacement sensitivity needed for the detection of gravitational waves.

3.1. Experimental Noise Sources

Several sources of noise must be considered in the design of a gravitational wave detector. The noise sources can be divided into two categories: displacement noise, which competes with the actual gravitational wave signal by causing unsought

motion of the experimental apparatus, and sensing noise, which is associated with the conversion of a small displacement into a readout signal.

A fundamental displacement noise source associated with the use of a macroscopic measurement apparatus is thermal noise, essentially collective modes of motion of components of the apparatus. Thermal noise is a generalization of Brownian motion, which arises from a coupling of a macroscopic element to its environment. According to the fluctuation-dissipation theorem (73), the displacement thermal noise of a component that can be modeled as an oscillator with effective spring constant k , mass m , and damping constant b can be described by

$$x_{\text{therm}}^2(f) = \frac{kTb}{\pi^2 f^2 (b^2 + (2\pi f m - k/2\pi f)^2)}. \quad 27.$$

The thermal noise peaks at the component resonant frequency ($= \sqrt{k/m}$) but also has an off-resonance tail. Thermal noise in the measurement band is limited by constructing components with a high quality factor Q (where Q is inversely related to the internal damping and is given by $2\pi f_0 m/b$) and with a resonant frequency outside the measurement band. As an example, a cylindrical fused silica optic with 30 kHz resonant frequency, 10 kg mass, and $Q = 10^7$ exhibits motion due to thermal noise of order 10^{-19} m/Hz^{1/2} at 100 Hz.

Another important displacement noise term is seismic noise due to the motion of the ground. Components of seismic noise are the earth's seismic background, man-made sources such as traffic and machinery, and wind and rain coupling to the ground through trees and buildings. The ground strain spectral density due to the earth's seismic background at 100 Hz, 1 Hz, and 10^{-3} Hz is roughly 10^{-14} /Hz^{1/2}, 10^{-12} /Hz^{1/2}, and 10^{-10} /Hz^{1/2}, respectively (74). Man-made sources of noise (e.g., traffic) may substantially increase these levels. This noise may be attenuated by a seismic filter, essentially an arrangement of a spring and mass with a low resonant frequency. Given a ground motion x_g , the motion transmitted through a filter above the resonant frequency f_0 is $x(f) \sim x_g (f_0/f)^2$. Filters may be stacked for large-multiple attenuations. Practical considerations limit f_0 to several hertz for passive filters, and several tenths of a hertz for actively controlled filters. At frequencies below 1 Hz, time-varying Newtonian gravity fields caused by earth motions and atmospheric fluctuations are also a serious limitation (75). Thus, below 1 Hz, a space-based measurement becomes an attractive possibility.

A fundamental type of sensing noise is shot noise. Shot noise occurs because granularity in currents causes fluctuations in counting rate and noise with a flat spectral density. For example, light arriving at the beamsplitter of an interferometer at a photon arrival rate r will have a variation in arrival number of $\sqrt{r\tau}$, where τ is the measurement interval. Because the light phase and photon number are conjugate variables, we find a phase variation $\Delta\phi = 1/\sqrt{r\tau}$ in the recombined light; this phase noise translates into a differential length error. Shot noise is minimized in this case by maximizing the photon arrival rate, or equivalently, the laser power. As an example, to enable a space-based displacement sensitivity of 10^{-12} m

(corresponding to 10^{-6} rad phase sensitivity) at 10^{-3} Hz, power of order 100 pW is required.

Another important sensing noise term is electronic noise. An important technique for the suppression of electronic noise is signal modulation—a signal can be modulated and then detected at a frequency sufficiently high to attenuate noise terms that decrease with higher frequency. Given a signal $S(f)$ competing with a noise term $n(f)$, modulation of the signal at a frequency Ω and averaging for a time interval $1/\Omega$ will give a signal-to-noise ratio of $S(f)/n(\Omega)$, so that the relative noise is greatly reduced. This technique is useful for sensing noise components such as electronic noise, but it does not reduce displacement noise associated directly with the signal.

3.2. Requirements and Principles of Detectors

3.2.1. RESONANT MASS DETECTORS Resonant mass detectors, or bar detectors, are long cylindrical masses whose fundamental vibrational mode is excited by the passage of a gravitational wave. The bar is constructed so that the resonant frequency f_0 is in an astrophysically interesting region. Practical considerations limit f_0 to ~ 1 kHz for an aluminum bar 1 m in length and 1 ton in weight.

The response of a bar of mass m , effective spring constant k , and damping term b to an external force F caused by the tidal acceleration of a gravitational wave is given by

$$G(f) = \frac{F/m}{\sqrt{(f_0^2 - 1/\tau_d^2 - (2\pi f)^2)^2 + (2\pi f b/m)^2}}, \quad 28.$$

where f_0 is $\sqrt{(k/m) - (b^2/4m^2)}$ and where τ_d , the bar decay time, is $2m/b$. The bar's response at resonance is proportional to the bar's Q . To maximize the bar sensitivity, we seek the highest possible Q (equal to $2\pi f_0 m/b$) and also seek to minimize the sensor and thermal noise.

The bar response in the time domain may be understood by considering its response $g(t)$ to a unit impulsive force applied to the mass,

$$g(t) \sim e^{-t/\tau_d} \sin(2\pi f_0 t), \quad 29.$$

which is that of a sinusoid decaying with characteristic time τ_d . The response of the bar to an arbitrary driving input (e.g., a gravitational wave) can be obtained by convolving the driving input with the bar impulse response.

The bar's motion is read out with a signal transducer, typically a SQUID (superconducting quantum interference device) accelerometer, which converts the bar's mechanical motion into an electrical signal. The bar and transducer form a system of coupled oscillators with two normal modes and two resonant frequencies; the most efficient energy transfer is obtained for a transducer with the same resonant frequency as the bar (76). Sensor noise can be reduced by using a long signal integration time.

Thermal noise presents a displacement noise limit to the bar sensitivity. The rms amplitude of oscillation due to thermal noise excitation is given by

$$x_{\text{rms}} = \sqrt{\frac{kT}{4\pi^2 m f_0^2}}. \quad 30.$$

This term, of order 10^{-16} m at room temperature, suggests that the bar should be operated at cryogenic temperatures. Also, because the time scale over which this rms motion takes place is of order τ_d (~ 300 s for $Q = 10^6$), the thermal noise may be further reduced with a signal integration time short compared to τ_d . Thus, the strategy for providing the lowest possible noise for a bar detector is to use a cold, high- Q material and choose a signal integration time that optimizes the tradeoff between sensor and thermal noise.

Finally, seismic noise at the bar resonant frequency must be suppressed to avoid unwanted excitation of the bar fundamental mode.

3.2.2. GROUND-BASED INTERFEROMETERS To enable sensitivity to a wide range of astrophysical gravitational wave sources, ground-based interferometers are designed to achieve strain sensitivity $\sim 10^{-21}$ over the audio band (10–5000 Hz); a maximum practical length of order 1000 m necessitates a displacement sensitivity of $\sim 10^{-18}$ m rms.

Ground-based interferometers are arranged in the Michelson configuration, which offers differential sensitivity to displacements along its orthogonal arms. The basic configuration uses a laser to inject light into the interferometer; the light is then split by a beamsplitter and directed along both orthogonal arms, which are defined by input and end test-mass optics. The light passes through the input test masses, reflects off the interferometer end test masses, travels back, and recombines at the beam splitter to interfere at a photodetector. The beamsplitter is set to maintain destructive interference of the light at the output port. Small differential length changes in the arms caused by the passage of a gravitational wave produce a relative phase shift in the arm light, which is seen as a change in intensity at the output photodetector. The total light travel time in the interferometer arms, τ_{arm} , is designed to be less than the period of a gravitational wave, to avoid loss of signal. Additional mirrors can be used to resonantly enhance the power of the interferometer stored light, reducing shot noise (77).

Key design features to limit noise couplings are as follows. The laser, of sufficiently high power to suppress shot noise, is stabilized in both intensity (to limit noise on the test masses from time-varying radiation pressure) and frequency (to limit wavelength fluctuations, which can appear as a length measurement error). The test masses are suspended from seismic attenuators, both to attenuate ground noise within the detection band and to limit slow ground motion that may disturb the interferometer operating point. Additional seismic isolation is provided by suspending the masses from pendula with resonant frequencies of order 1 Hz. Careful attention is paid to the optical material and attachments to the optics that

could cause loss and increase thermal noise. Finally, the interferometer is placed within a vacuum system to remove air density fluctuations and acoustic noise.

An ultimate limit to the performance of ground-based detectors is imposed by gravity gradient noise, caused by earth motion and time-varying atmospheric conditions, from which the test masses cannot be shielded.

3.2.3. SPACE-BASED INTERFEROMETERS An interferometer placed in space offers the immediate advantages of an absence of seismic noise, a highly stable thermal environment, and the presence of a vacuum. The low-noise environment, along with the very long arm lengths that are possible in space, allow for strain signal sensing at much lower frequencies and at higher displacement levels than is possible with a ground-based system. An arm length of order 10^9 m allows sensing at a frequency of 1 mHz and yields strain sensitivity of 10^{-21} with a displacement sensitivity of only (!) 10^{-12} m.

A Michelson interferometer configuration is formed in space by using three spacecraft placed on the vertices of an equilateral triangle, each sending and receiving a laser beam to and from its neighbors. Because the transmitted beam spreads through diffraction over long travel distances, there is insufficient power to reflect the beam back to its starting point; thus, a transponding scheme is used, in which an onboard laser at a far spacecraft is phase locked to the incoming beam and sends its light back to the initial spacecraft.

Key sensing noise sources are the following. At high frequencies, strain sensitivity is limited by shot noise. Shot noise is set by the power received at each vertex spacecraft, which in turn depends on the output laser power and the attenuation of the transmitted beam. Also, frequency noise of the laser is a particular problem for space based-detectors because it couples to the long arm length. Although the Michelson configuration is first-order insensitive to frequency noise, small fractional differences in the arm lengths must be accounted for by time-shifting the phase signals from the arms.

Because the space-based detectors operate at low frequencies, small-force noise sources produce relatively large displacement noise. Although the proof masses are shielded from noise by the surrounding spacecraft, relative motion of the spacecraft and proof mass will lead to gravitational, electrical, and magnetic disturbances of the proof mass. Thus, the separation between the spacecraft and the proof mass must be held constant. This is achieved by a drag-free control system that consists of a sensor, thruster actuator, and feedback control system.

3.2.4. DOPPLER TRACKING OF SPACECRAFT Doppler tracking is performed by sending a radio signal to a distant spacecraft, which coherently transponds a signal back to the earth (78). By comparing the frequency of the transmitted and received signals, one can measure the Doppler shift and thereby search for the perturbation of the spacecraft-earth distance caused by gravitational waves. The large possible separation between a spacecraft and the earth permits sensitivity to gravitational waves at a frequency range down to 10^{-6} Hz.

TABLE 2 Characteristics of resonant mass detectors

Characteristic	ALLEGRO	AURIGA	EXPLORER	NAUTILUS	NIOBE
Material	AL5056	AL5056	AL5056	AL5056	Nb
Mass (kg)	2296	2230	2270	2260	1500
Length (m)	3.0	2.9	3.0	3.0	2.9
$Q \times 10^6$	2	3	1.5	0.5	20
f_0 (Hz)	920 895	930 912	921 905	924 908	713 694
Δf (Hz)	1	1	9	1	1
Temperature (K)	4.2	0.2	2.6	0.1	5.0
Sensitivity ($\text{Hz}^{-1/2}$)*	1×10^{-21}	2×10^{-22}	1×10^{-21}	2×10^{-22}	8×10^{-22}

*The sensitivity is the bar strain noise amplitude spectral density at its resonant frequency.

The primary noise source is frequency dispersion from fluctuating plasma density in the solar wind and earth atmosphere (79). These backgrounds may be measured and attenuated with the use of multiband radio transmission.

3.3. Descriptions of Facilities

3.3.1. RESONANT MASS DETECTORS A number of cryogenic bar detectors have been operated around the world, including ALLEGRO (80) (Baton Rouge, Louisiana, United States), AURIGA (81) (Padova, Italy), EXPLORER (82) (CERN), NAUTILUS (83) (Rome, Italy), and NIOBE (84) (Perth, Australia). The characteristics of the bars throughout a data-taking period from 1997 through 2000 are summarized in Table 2, including mass, length, resonant frequency, Q , bandwidth, and strain sensitivity (85). The bars were all equipped with a SQUID amplifier coupled with a resonant transducer, with the exception of the NIOBE detector, which used a microwave cavity.

The bar detectors listed in Table 2 share many characteristics. Figure 6 shows the seismic isolation system of the ALLEGRO bar detector, which yields the large attenuation factor shown (86). Other bars employ similar seismic isolation systems.

An active area of research on bar detectors involves raising the bandwidth by lowering the transducer and amplifier noise. The relatively high bandwidth of the EXPLORER detector is due to a special transducer design that allows a very small gap size and high coupling to the bar. A recent advance in this area has been achieved by the NAUTILUS group, which has obtained a 100 Hz detector bandwidth.

3.3.2. GROUND-BASED DETECTORS Ground-based detectors include LIGO, VIRGO, GEO, and TAMA.

3.3.2.1. LIGO The LIGO observatory consists of one site in Livingston, Louisiana (LLO) and another in Hanford, Washington (LHO). The independent

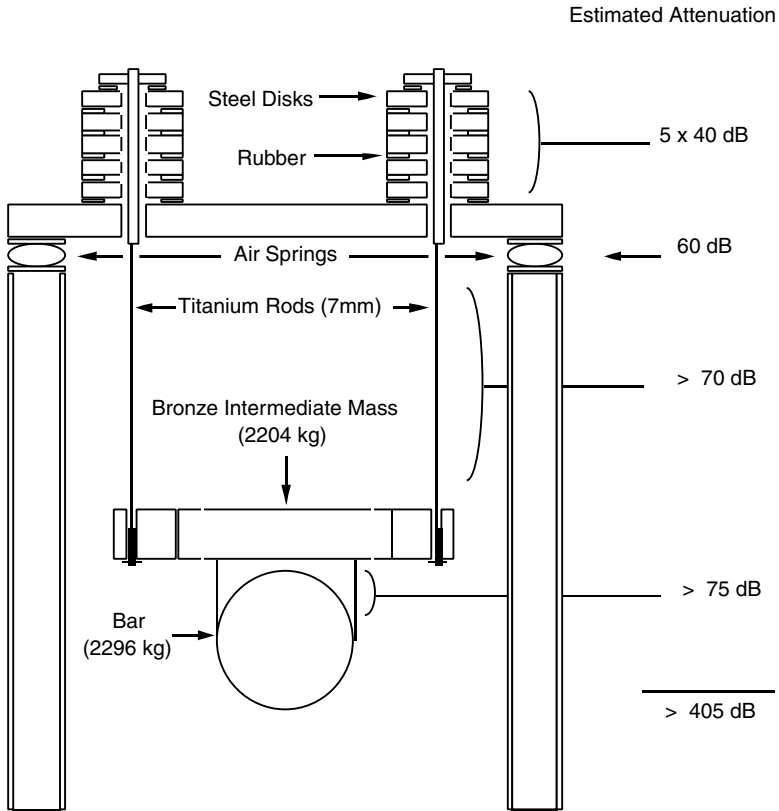


Figure 6 Seismic isolation in the ALLEGRO bar detector (from Reference 86 with permission).

measurements of the two sites are essential to distinguish a gravitational wave signal from noise (87, 88). Figure 7 shows an aerial view of LHO; the vacuum beam tubes that allow the light to propagate through its 4 km arms can be seen intersecting at the vertex area, which contains the laser, beamsplitter, and input test masses.

LLO has one 4 km interferometer (referred to here as L1), whereas LHO incorporates one 4 km and one 2 km interferometer (referred to as H1 and H2) that share the same vacuum system. The interferometers at both sites are aligned to within 18° (modulo 90). Figure 8 shows a schematic layout of the LIGO interferometer, including input laser, and beam splitter and test mass optics.

The LIGO H1 detector is configured as follows. The laser system consists of a neodymium:YAG laser of $1.06 \mu\text{m}$ wavelength and 10 w output power. At a frequency of 100 Hz, the laser intensity is stabilized to 1 part in 10^8 by measuring its fluctuations with a quiet photodetector, and its frequency is stabilized to 1 part in 10^{12} by comparing its wavelength to the length of a fixed optical cavity (89). The light is further stabilized by a 24 m suspended triangular cavity (called a

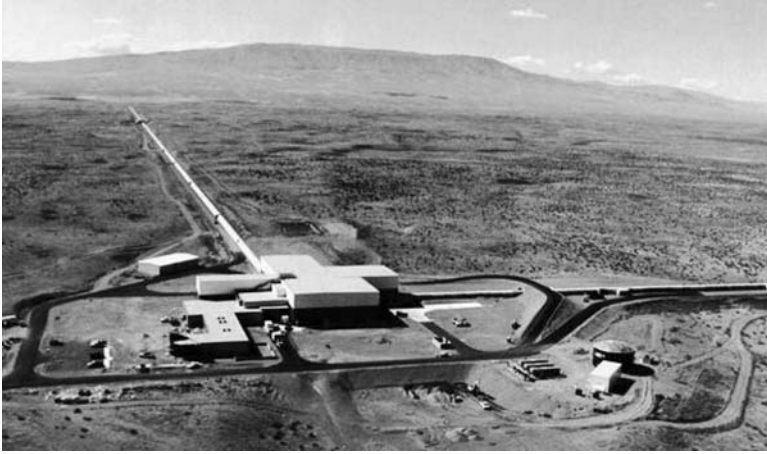


Figure 7 Aerial view of the LIGO Hanford site (LHO), showing the vertex building and orthogonal beam tubes.

“mode cleaner,” not shown in Figure 8) that removes pointing fluctuations (90) and provides additional frequency stabilization to the laser. After exiting the mode cleaner, 6 w of light enters the interferometer.

The interferometer comprises six large optics: the recycling mirror, which resonantly enhances the interferometer’s stored light power level by directing light returning to the laser back to the beam splitter (77); the beamsplitter, which directs

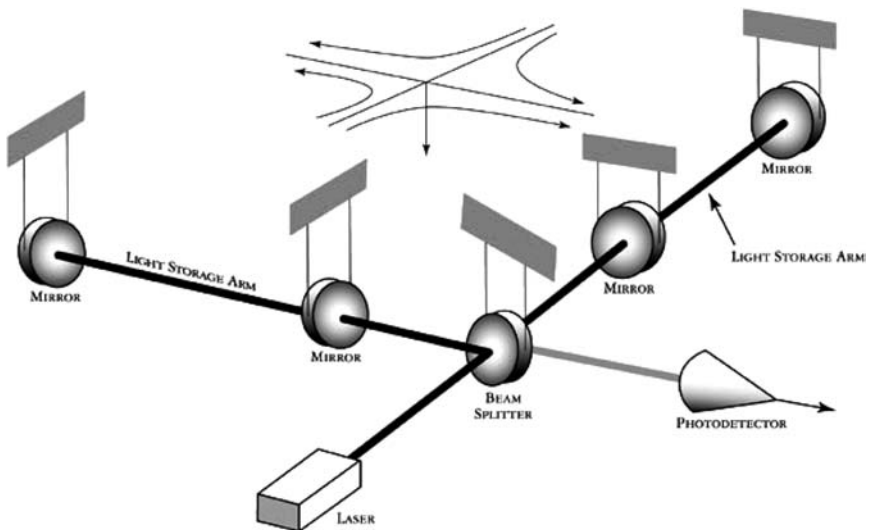


Figure 8 Schematic view of the LIGO detector, including laser, test mass optics, beam splitter, and photodetector.

the light to the arm cavities; and two input and two end test masses, which define the 4 km interferometer arms (91). The test masses have stringent optical specifications: <50 ppm scatter, <5 ppm/cm absorption, and ~ 1 nm rms deviation from sphericity (92). The controlled lengths of the arm cavities allow the laser light to resonate, forming Fabry-Perot resonators (93) that increase the storage time of the light by a factor of 60 relative to a single trip through the arm. This allows the light to interact with a gravitational wave for a correspondingly longer time, developing an enhanced phase shift and allowing the required shot noise level to be reached. The test masses are shaped with radii of curvature of order 10 km to form stable resonators over the 4 km arm length.

The interferometer is kept in stable resonance with the aid of a length control system, which suppresses motion due to low-frequency seismic noise and keeps the test masses positioned to a differential precision of order 10^{-13} m rms (94), and an alignment control system, which uses a wavefront-sensing technique to keep the test masses aligned to the interferometer optical axis to $\sim 10^{-8}$ rad rms (95). These controls are necessary to stabilize the interferometer operating point and to prevent coupling of higher-frequency technical noise sources to the gravitational wave signal. Final frequency stabilization from the arm cavities back to the laser results in a frequency stability of 1 part in 10^{21} at 100 Hz (94).

The signal is read out using a phase modulation technique (also known as Pound-Drever-Hall locking), which adds radiofrequency sidebands to the carrier signal and monitors the phase difference between the two frequencies at the interferometer differential output to sense the relative arm length displacement (96).

Finally, the interferometer optics and mode cleaner are held in place by suspensions that support the optics with a steel wire pendulum and control them with attached magnets and coil drivers. The suspension is itself supported by the seismic attenuation system, which uses four stacks of spring-mass filters to attenuate seismic noise (97). The resonant frequency of the suspension and seismic stack are approximately 1 Hz and 2 Hz, respectively, and provide a combined attenuation of 10^{12} at 100 Hz. The very high dependence of the attenuation factor on frequency means the interferometer sensitivity is limited by seismic noise below 40 Hz. Thermal noise of the pendulum, due to mechanical loss in the wire and attachments, limits the interferometer sensitivity between 40 and 200 Hz. Above 200 Hz, shot noise is the limiting noise source.

The contributions of seismic, thermal, and shot noise to the LIGO noise budget are shown in Figure 9. The figure also shows other noise sources, including stray light, fluctuating optical pathlengths from residual gases in the vacuum system, and gravity gradient noise due to atmospheric disturbances, etc.

3.3.2.2. VIRGO The VIRGO observatory (98) is operated by a French and Italian collaboration and located in Cascina, Italy. It consists of one 3 km interferometer. It shares many characteristics with LIGO, including a 10 W stabilized laser system, an input mode cleaner, resonant arm cavities, length and alignment control systems,

and large precision optics. The most prominent difference between LIGO and VIRGO is the seismic attenuation system: VIRGO's "superattenuator" design (99) consists of a chain of five filters composed of blade springs and damping magnets, which provide 10^{15} -fold attenuation of seismic noise at 10 Hz. This degree of isolation suppresses seismic noise below thermal noise at frequencies above 4 Hz, thus significantly improving low-frequency performance. Other VIRGO features include an output mode cleaner that allows the test mass surface specification to be reduced to ~ 10 nm rms. VIRGO's design sensitivity is comparable to LIGO's at frequencies greater than 100 Hz and is better by a factor of ~ 100 at 10 Hz.

3.3.2.3. GEO The GEO facility (100), run by a collaboration of Germany and the United Kingdom, is located in Hanover, Germany. Figure 10 shows a schematic layout of the GEO600 interferometer. GEO uses a 600 m interferometer with a 10 W stabilized laser, two input mode cleaners, and two bounce delay lines for arms. Its design includes the use of a signal recycling mirror that causes the differential gravitational wave signal to resonate in the interferometer (101); the resonance is frequency-dependent, providing the possibility of an increase in sensitivity at the resonant frequency at the expense of reduced interferometer bandwidth. The resonance can also be tuned to frequencies of interest. GEO uses a triple pendulum to suspend its optics, with the final stage consisting solely of high- Q fused silica (102). This results in lowered thermal noise as well as additional low-frequency seismic isolation. Because of its significantly shorter length, GEO's sensitivity is a factor of ~ 8 lower than LIGO's across its full band, but its tunability allows it to reach the LIGO sensitivity at selected frequencies.

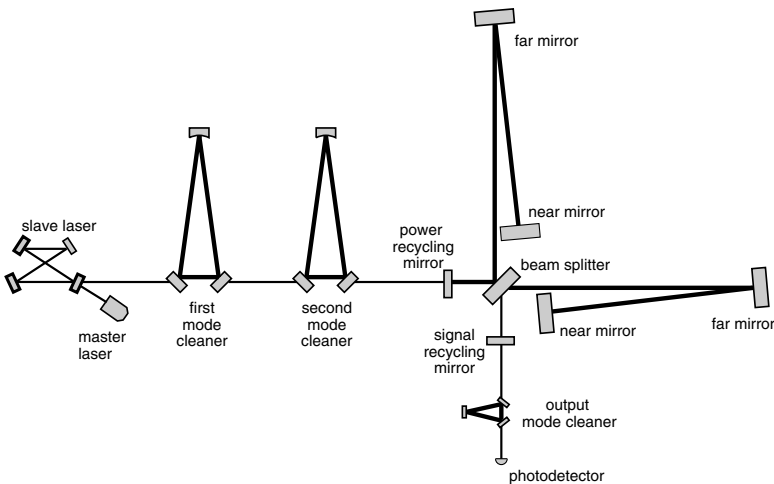


Figure 10 Schematic view of the GEO detector, including input and output mode cleaners and signal recycling mirror to allow tuning of interferometer sensitivity.

3.3.2.4. TAMA The TAMA detector (103) is located in Tokyo, Japan. Its configuration is similar to that of the LIGO detector, with a power recycling mirror and resonant arm cavities, and its length is 300 m. In addition to searching for gravitational waves, the commissioning and operation of TAMA is considered essential to the proposal of an advanced cryogenic interferometer, described below.

3.3.3. LASER INTERFEROMETER SPACE ANTENNA LISA (104) consists of three spacecraft placed at the vertices of an equilateral triangle, with arm length of 5×10^9 m. Each spacecraft houses two proof masses that define the arm lengths and two lasers that transmit light to neighboring spacecraft (Figure 11). By monitoring the phase difference between local light and that received from a far spacecraft, each spacecraft can perform an interferometric comparison of length variations of its two arms. The spacecraft configuration will orbit the sun 20° behind the earth, with the plane of the triangle inclined at 60° with respect to the elliptic, as shown in Figure 12. This orbit provides a very stable thermal environment for the constellation. LISA will slowly rotate once per year, imposing amplitude, frequency and phase modulation of the gravitational wave signal so that the source location can be extracted.

Light is transmitted from local to far spacecraft with the use of a Nd:YAG 1 W laser beam expanded through a telescope of 30 cm diameter. The laser is amplitude- and frequency-stabilized at 1 mHz to levels of 1 part in 10^6 and 10^{12} , respectively, to limit radiation pressure noise, as well as length noise from residual frequency fluctuations (105). The far spacecraft laser is phase locked to the incoming light and then sends its light back to the initial spacecraft. Diffraction of the propagating beam will leave 100 pW of light to be collected back at the local spacecraft, imposing a shot noise limit of $20 \text{ pm/Hz}^{1/2}$ sensitivity at frequencies above 1 mHz in the length measurement. The local and far light beams are then compared in phase to extract a time-varying length measurement. An identical measurement is performed for the other interferometer arm. However, before the two length measurements can be compared, the coupling of frequency noise to the differences in arm path lengths ($\sim 1\%$ of the arm length) must be accounted for. This is done by time-shifting the arm data streams relative to each other, a procedure known as time-delay interferometry (TDI) (106). A limitation to the effectiveness of TDI is the uncertainty in the knowledge of the arm lengths, of order 50 m, obtained from spacecraft tracking.

Details of the LISA interferometer are shown in Figure 13, with a view of the proof mass, optical bench, and beam expanding telescope (104).

Although the spacecraft shields the proof masses from external disturbances, the distance from spacecraft to proof mass must be kept stable at the level of $3 \text{ nm/Hz}^{1/2}$ at frequencies down to 0.1 mHz; otherwise, Newtonian gravity gradients and other position-dependent noise couplings will perturb the mass. Stability is maintained by a drag-free control system, which uses capacitive sensors to measure displacements of the spacecraft with respect to the proof mass and micronewton thrusters to control the spacecraft's position and keep the displacement

constant (104, 105). The drag-free technology required for the operation of LISA will be tested at 10 times the required LISA level in a flight demonstration mission planned for 2007 (107).

A number of additional external noise sources on the proof mass must be limited to 10^{-15} nt/Hz^{1/2} down to 0.1 mHz. This force level produces a 10^{-12} m disturbance over a 1000 s interval. To limit differential radiation pressure on the proof mass, thermal stability of 60 microKelvin/Hz^{1/2} at 0.1 mHz is needed; this is accomplished with the constellation orbit shown in Figure 12 and three layers of passive thermal shielding (104). A vacuum level of 10^{-8} torr limits fluctuations in gas pressure on the proof mass (108). Charging effects are suppressed by periodic discharge of the mass. Finally, spatial and temporal variations in the proof mass surface potential (the “patch effect”), which can couple to DC voltage offsets between the mass and sensor, are limited by the use of a gold coating to maintain a very clean surface (105, 109). These and other noise couplings are studied on the ground with the use of a torsion pendulum, a device with a low resonant frequency (3 mHz) and very soft rotational restoring force (110). Thermal noise in its tungsten suspension wire limits its force sensitivity to roughly 100 times the required LISA level. Some recent work with coated, conductive fused silica fibers offers the possibility of a torsion pendulum with sensitivity closer to the LISA force noise requirement (K. Numata, J. Gundlach, private communication).

The planned LISA sensitivity curve is shown in Figure 2. Shot noise is the dominant noise source above 10 mHz; the sum of the force noise elements described above are limiting below 2 mHz.

3.4. Planned Facility Upgrades

3.4.1. SPHERICAL RESONANT MASS DETECTOR The possibility of using a spherical resonant mass detector for the detection of gravitational waves is under study by several groups (112). A spherical detector offers the following advantages. First, the direction and polarization of a gravitational wave from any direction can be determined by using five transducers on the sphere to monitor the amplitude of its five quadrupole modes of vibration. Also, at the same resonant frequency, the sphere has 70 times the gravitational wave detection cross section of a bar due to its larger mass and omni-directionality. A prototype spherical detector of 70 cm diameter is now under construction at Leiden University in the Netherlands (113).

3.4.2. ADVANCED LIGO The LIGO collaboration has proposed a detector upgrade that would provide roughly a tenfold increase in sensitivity across a wider detection band (114). The upgrade is currently proposed to begin around 2007, with the goal of completing the initial commissioning in 2010. The greater sensitivity of this detector, known as the advanced LIGO, would allow the detection rate to increase by a factor of > 1000, assuming isotropic distribution of sources.

The advanced LIGO owes its increased sensitivity to the following technical upgrades of its subsystems. In the proposal, a 200 W laser provides a light power of 120 W at the input to the interferometer, reducing shot noise. Active seismic isolation allows seismic attenuation of order 10^3 at 1–10 Hz, and significant attenuation down to 0.1 Hz. Quadruple pendula are used to suspend the optics, lowering the suspension thermal noise. The optics are made of sapphire, a material with higher Q and higher density than fused silica, to decrease optic thermal noise and the noise from radiation pressure. Finally, the advanced LIGO will incorporate a signal recycling mirror to allow tuning of its sensitivity.

Figure 5 shows the relative sensitivity of the initial and advanced LIGO interferometers.

3.4.3. THIRD-GENERATION GROUND-BASED DETECTORS Two detectors now under study would offer higher sensitivity than the advanced LIGO. The Large-Scale Cryogenic Gravitational Wave Telescope (LCGT) (115) is a 3 km facility planned for installation in an underground mine in Kamioka, Japan. It would resemble the advanced LIGO in design but would also use cryogenics to cool its test masses and suspensions to 20 K. This would reduce the suspension and optic thermal noise so that the strain sensitivity would be two- to threefold higher than that of the advanced LIGO over all of its detection band. To examine the difficult technical issues associated with cooling a suspended mass interferometer, a 7 m interferometric cryogenic facility has been built at the Institute for Cosmic Ray Research in Tokyo, Japan (116).

An ambitious interferometer named EURO has been described in a vision paper submitted to the funding agencies of Britain, France, Germany, and Italy (www.astro.cf.ac.uk/geo/euro/euro.pdf). The goal of research for EURO would be to pioneer and employ many advanced interferometric techniques leading to quantum noise limited performance, including cryogenically cooled optics, necessary to minimize thermal noise; kilowatt-power-level lasers; and diffractive optics, which would direct laser light by diffraction through gratings to avoid the thermal deformations associated with absorption on reflective surfaces. EURO envisions a sensitivity increase of ~ 10 beyond that of the advanced LIGO, as well as an extension of bandwidth by about a factor of 10 at both low and high frequencies.

3.4.4. BIG BANG OBSERVATORY The Big Bang Observatory (BBO; <http://universe.gsfc.nasa.gov/be/roadmap.html>) is a follow-on mission to LISA, a vision mission of NASA's "Beyond Einstein" theme. BBO will probe the frequency region of 0.01–10 Hz, a region between the measurement bands of the presently funded ground- and space-based detectors. Its primary goal is the study of primordial gravitational waves from the era of the big bang, at a frequency range not limited by the confusion noise from compact binaries discussed above. In order to separate the inflation waves from the merging binaries, BBO will identify and subtract the signal in its detection band from every merging neutron star and black hole binary in the universe. It will also extend LISA's scientific program of measuring waves

from the merging of intermediate-mass black holes at any redshift, and will refine the mapping of space-time around supermassive black holes with inspiraling compact objects.

The strain sensitivity of BBO at 0.1 Hz is planned to be $\sim 10^{-24}$, with a corresponding acceleration noise requirement of $< 10^{-16}$ m/(s² Hz^{1/2}). These levels will require a considerable investment in new technology, including kilowatt-power-level stabilized lasers, picoradian pointing capability, multi-meter-sized mirrors with subangstrom polishing uniformity, and significant advances in thruster, discharging, and surface potential technology.

4. DATA ANALYSIS

In this section, we review the analysis strategies for searching for faint gravitational wave signals and the data-analysis efforts to date.

4.1. Data-Analysis Techniques

4.1.1. MATCHED FILTERING If the waveform of a particular source is known, the optimal method for searching for the waveform in noisy data is the matched filter (119). Let $k(t|\theta)$ represent the template that describes the gravitational wave signal in the detector for a source with parameters θ . (For example, we may be searching for the inspiral signal from a coalescing neutron star binary system, in which case θ represents the component masses.) If $s(t|\bar{\theta}) = h(t|\bar{\theta}) + n(t)$ is the (noisy) measurement of a gravitational wave signal with parameters $\bar{\theta}$, then the correlation between the detector output and the template is defined as

$$\langle s(\bar{\theta})|k(\theta) \rangle = 2 \int_0^{\infty} \frac{\tilde{s}(f|\bar{\theta}) \tilde{k}^*(f|\theta) + \tilde{s}^*(f|\bar{\theta}) \tilde{k}(f|\theta)}{S_n(f)} df, \quad 31.$$

where $S_n(f)$ is the strain noise power spectral density $\tilde{s}(f)$ and is the Fourier transform of $s(t)$. The filter (Equation 31) correlates the time-series data with the template (numerator), emphasizing the frequencies where the noise is low relative to frequencies where the noise is high (denominator). The signal-to-noise ratio of the matched filter is given by

$$\rho(\theta, \bar{\theta}) = \frac{|\langle s(\bar{\theta})|k(\theta) \rangle|}{\langle k(\theta)|k(\theta) \rangle^{1/2}}. \quad 32.$$

The best-fit parameters are found by maximizing $\rho(\theta, \bar{\theta})$. When ρ exceeds an appropriate threshold ρ^* , a candidate signal has been identified. Owing to the presence of noise, the best-fit parameters will not necessarily correspond to the true source parameters $\bar{\theta}$.

Matched filtering is used extensively in the search for inspiral signals from neutron star or black hole binary coalescence. The waveforms that describe the in-

spiral gravitational radiation are well approximated by a post-Newtonian expansion (120) and may be used to generate the matched filter. In practice, the matched filter output is calculated simultaneously for a large number of different templates (i.e., different θ) that span the space of expected signals.

This technique is also important in extracting a signal from the noisy background of bar detectors. In this case, a matched filter is applied for gravitational wave burst signals observed with an optimal averaging time (as discussed in Section 3.2.1). The filter serves to deemphasize thermal noise close to the bar resonance.

4.1.2. TIME-FREQUENCY ANALYSIS In the search for many sources of gravitational radiation, including black hole mergers and core collapse of massive stars, the waveforms are not known with sufficient accuracy to allow the use of matched filtering. In these cases, methods are used that look for evidence of gravitational radiation without a priori knowledge of the waveform.

One important technique employs time-frequency decomposition of the detector data. In this analysis, slices of the data are taken at fixed time intervals, and a Fourier decomposition of each slice is done. Comparison of the power present in a given frequency interval as a function of time, relative to the known statistical distribution of the noise power, will indicate the possible presence of a gravitational wave.

This approach has several variants. The excess power method compares power in an estimated frequency band for an estimated duration to the known statistical distribution of noise power (121). If the detector noise is stationary and Gaussian, the noise power will follow a chi-squared distribution with the number of degrees of freedom equal to twice the time-frequency volume. Thus, the efficacy of this method to detect the excess power related to a gravitational wave signal depends on the expected duration and bandwidth of the signal as well as its strength. A related method, TFCLUSTERS, searches for clusters of pixels in the time-frequency plane with power above a given threshold (122). Because most signals have pixels with a high degree of spatial correlation in the time-frequency plane, this type of clustering analysis is useful to filter out detector noise. An example is shown in Figure 14.

4.1.3. CHANGE-POINT ANALYSIS Another method for identifying a signal without knowledge of the waveform is to look for a change in the statistics of the detector output in the time domain. The approach is to divide the data into blocks within which the statistics are approximately constant. The statistics of each block are then characterized by the parameters of normal distributions, mean and variance. A “change point” is defined as a time when the noise character changes, so that probability of the data to either side of the point belonging to different distributions exceeds a determined threshold (123). The identified change points thus define the blocks, characterized for start and end times, mean, and variance.

Once blocks of varying mean and variance are determined, adjacent unusual blocks are clustered into a single event. Coincident analysis between separate detectors can then be performed, including frequency band, time of loudest block, calibrated energy, and duration.

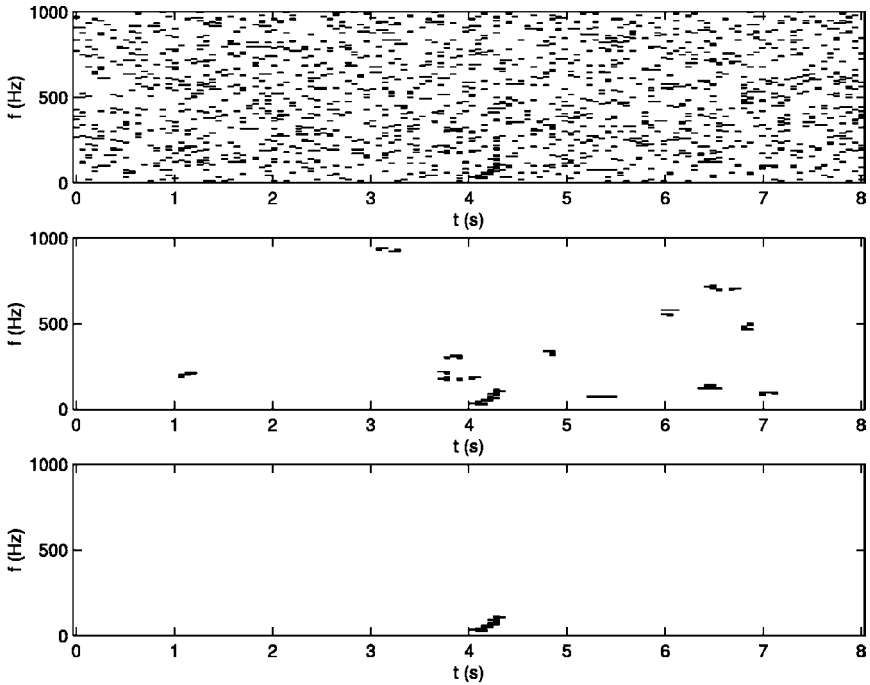


Figure 14 Time-frequency analysis applied to a simulated binary chirp in a white Gaussian noise background. The first plot (*top*) is the result of a threshold applied to the power of the pixels of a time-frequency decomposition of the data. The second plot (*center*) retains clusters of pixels with common sides. The final plot (*bottom*) applies a threshold to the total power of the clusters. (From Reference 122 with permission.)

4.1.4. CORRELATION AND COINCIDENCE TECHNIQUES Correlation of the signals from more than one detector is critical for suppressing noise and allowing a real signal to be identified. With $t_1 = t_2 + L/c$, where t_1 and t_2 are the recorded time at each detector and $L = |(\vec{x}_1 - \vec{x}_2) \cdot \hat{n}|$ is the projected distance between detectors for a source in the \hat{n} direction, we can form the detector cross correlation Y :

$$Y \equiv \int_{-T/2}^{T/2} dt_1 \int_{-T/2}^{T/2} dt_2 s_1(t_1) Q(t_1 - t_2) s_2(t_2), \quad 33.$$

where s is the detector strain output and Q is a filter that can be chosen to maximize the signal-to-noise ratio of Y for a given expected signal. To find the optimal $Q(t)$, we assume that the detector noise is stationary, Gaussian, and uncorrelated between different detectors. This approach is used to search for the expected low stochastic background signal.

A measurement of the signal from multiple detectors also allows identification of the source position. Measurement of the signal with two detectors locates the

source within a circle on the sky, with the angle of declination relative to the polar axis (defined by an extension of the baseline between the detectors) given by $\theta = \cos^{-1}(c\Delta t/D)$, where Δt is the time difference between the detected signals and $D = |\vec{x}_1 - \vec{x}_2|$ is the distance between the detectors (124). Use of a third detector gives two position circles that intersect at two patches on the sky, and a fourth detector localizes the source to within a single patch. With a timing resolution of 0.1 ms and detectors in the United States, Europe, and Japan, a localization of ~ 20 arcmin is possible.

4.1.5. PULSAR TIMING ANALYSIS Pulsars are excellent clocks. For example, the period of millisecond pulsar B1937 + 21 has been measured to 1 part in 10^{13} . Thus, pulsar timing measurements can be used to infer the existence of gravitational waves through the observation of the modulation of the pulsar signal. The strain sensitivity possible with an array of timing devices is given by (125) $h \sim R/(N^{1/2}T/2\pi)$, where R is the residual from the timing model, N is the number of devices in the array, and T is the measurement duration. A pulsar timing array is particularly suitable in the search for gravitational waves in the frequency range 10^{-9} to 10^{-7} Hz, where noise limits the performance of the ground- or space-based interferometric systems.

The timing of pulsar signals allows the study of gravitational waves in a number of different ways. First, monitoring the orbital decay supplies information on the luminosity of the waves, as in the case of the Hulse-Taylor binary pulsar, PSR B1913+16. Second, the effect of low-frequency gravitational radiation on the periodic modulation of the arrival time of the pulsar signal can be observed, allowing the identification of gravitational waves from supermassive black hole binaries and stochastic backgrounds.

4.2. Ground-Based Interferometer Results

The results shown in this section were obtained from the LIGO S1 science run, taken during a 17-day period starting in August 2002 (126). The analysis of this run offers the highest-sensitivity performance of a wide-band gravitational wave interferometer to date.

Figure 15 shows the detector sensitivity during the S1 run, as well as the sensitivity during the following two science runs, S2 and S3 (<http://www.ligo.caltech.edu>). The notable improvement in interferometer performance with time is due to the ongoing commissioning activity to fully implement the LIGO design. Data from the S2 run is presently under analysis. The durations of the S2 and S3 runs were 59 and 66 days, respectively. At the time of the S1 run, the interferometer alignment system was not yet fully implemented and the laser frequency and intensity were not fully stabilized. In addition, the laser was not run at full power. Because the detector sensitivities were several orders of magnitude away from the design goal, data analysis was not expected to result in source detections. Rather, the analysis was undertaken to provide upper limits

of astrophysical interest, while establishing the methodology of gravitational wave data analysis by using the algorithms described above to treat actual data.

The data-taking rate of the gravitational wave channel was 16 kHz. The strain signal was calibrated at the 10% level with a swept sine-wave modulation of the detector arm length. Data taking took place with the interferometer operating in “science mode,” a state characterized by an absence of excess noise from mechanical resonances excited by large control system transients. Detector duty cycles for this run were between 40% and 70%, limited by impulsive seismic events from man-made sources (e.g., traffic).

The interferometer analysis described in Section 4.2 was done within the LIGO Scientific Collaboration, a worldwide association of scientific groups that carries out the scientific program of the LIGO laboratory. Subgroups address the burst, inspiral, stochastic, and pulsar analyses of the following sections.

4.2.1. BURSTS A search for linearly polarized gravitational wave bursts of short duration (4–100 ms) was undertaken, using a time-frequency decomposition of the strain data (128). No assumptions were made about the nature of the burst.

To minimize the rate of false events from fluctuations in the detector noise, a coincidence between all three detectors was required for the identification of a burst event. After exclusion of stretches of data where the noise in the gravitational wave channel exceeded a predetermined threshold, a total of 35.5 h of triple-coincidence observation time remained for analysis. The TFCLUSTERS algorithm, described above, was used to search for signals above the detector noise background. The number of events observed was consistent with expectations for random accidental coincidences from detector noise, estimated by time-shifting the data from different detectors, and was less than 2 events/day.

The efficiency of the search algorithm was determined by injecting simulated signals into the data stream. These included Gaussians of the form $h = h_0 \exp(-t^2/\tau^2)$, with a range of durations; and sine Gaussians, of the form $h = h_0 \sin(2\pi f_0 t) \exp(-t^2/\tau^2)$, with a ratio of frequency width to central frequency of 9, and a range of central frequencies. The results are shown in Figure 16, which plots the event rate versus the root-sum-square amplitude spectral density, defined by $h_{rss} = \sqrt{\int |h|^2 dt}$. The upper limits shown are for an ensemble of waves of equal amplitude, incident on the earth from all directions and with all linear polarizations.

4.2.2. BINARY NEUTRON STAR INSPIRAL The detectors in the S1 run were sensitive to inspiral events (at a signal-to-noise level of 8) to a maximum distance between 30 and 180 kpc. Candidate inspiral events were determined through the application of matched filters that covered the mass range 1–3 M_{\odot} , as well as the starting orbital phase and the inclination of the orbit relative to the plane of the sky (129). The matched filter technique used in this analysis assumed stationarity of the noise spectrum over periods of several minutes; however, the state of commissioning of the interferometer during the S1 run was such that brief periods of excess broadband noise in the interferometer led to the generation of spurious events.

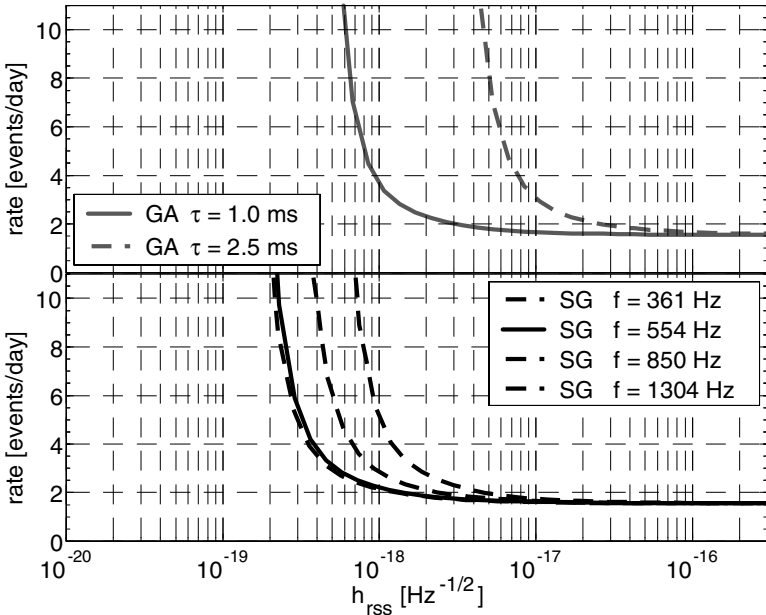


Figure 16 Burst upper limits for Gaussian and sine-Gaussian waveforms. h_{rss} is the root-sum-square amplitude spectral density of the burst. (From Reference 128 with permission.)

These transient noise artifacts that excited the matched filter were rejected by requiring a time–frequency examination of the accumulation of the signal-to-noise ratio of the chirp signal. An additional veto related to the observation of very-high-broadband detector noise was also used.

The analysis used coincidences from triggers from the LLO 4 km and LHO 4 km detectors (the LHO 2 km detector noise was found to show excessive non-stationarity and was not used in this search). To increase the visible distance and observation time, when coincidences were not available a single detector was used, with the caveat that events identified this way could not be used as evidence of gravitational wave detection—only to set an upper limit.

Because no model existed for the level of background events in each detector, an approach was chosen that identified the event with largest SNR in the data and calculated an upper limit assuming no background above this level. For a Poisson-distributed set of events of rate R , the probability P of observing an inspiral signal in observation time T with SNR of $\rho > \rho^*$ is

$$P(\rho > \rho^*) = 1 - e^{-RT\varepsilon(\rho^*)}, \quad 34.$$

where ε is the detection efficiency. An upper limit at 90% confidence level (CL) is then given by $R_{90\%} = 2.3/[T\varepsilon(\rho^*)]$. The efficiency of the search was obtained by

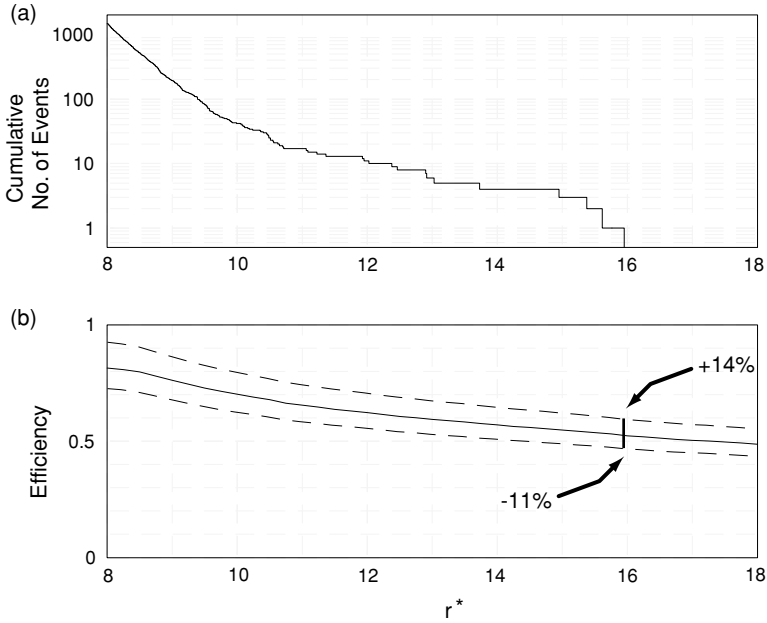


Figure 17 Neutron binary inspiral loudest event and detection efficiency. ρ is the signal-to-noise ratio of the event. (From Reference 129 with permission).

the injection of simulated inspiral signals into the data stream (see Figure 17). The upper limit obtained for 214 h of data was $R_{90\%} < 1.7 \times 10^2$ per year per Milky Way equivalent galaxy (MWEG). This limit is a factor of 26 lower than that of the best previous search and is the best observational limit to date, although much higher than the best current theoretical prediction of $2 \times 10^{-4}/y/MWEG$.

4.2.3. STOCHASTIC BACKGROUND The stochastic background is sought by correlating the outputs of the detectors (130). With the assumption that the detector noise is Gaussian, stationary, and uncorrelated between different detectors, the expected value of the cross correlation Y depends only on the stochastic strain signal S_{gw} :

$$\langle Y \rangle = \frac{T}{2} \int_{-\infty}^{\infty} df \gamma(f) S_{\text{gw}}(f) Q(f). \tag{35}$$

Here $\gamma(f)$ is a function that characterizes the reduction in sensitivity due to the space-time separation, as well as the relative orientation of the two detectors, and T is the measurement time. $Q(f)$ is a filter function chosen to maximize the signal-to-noise ratio $\rho = Y/\sigma_y$, where σ_y is the variance of Y and is related to the detector noise:

$$\sigma_Y^2 = \frac{T}{4} \int_{-\infty}^{\infty} df S_{n1}(f) |Q(f)|^2 S_{n2}(f), \quad 36.$$

where S_{n1} and S_{n2} are the strain noise power spectra of the two detectors.

For this analysis, which assumed a stochastic background with $\Omega_{\text{gw}}(f) = \text{constant}$ over the LIGO band, the strain signal falls as $1/f^{3/2}$ (see Figure 18a). The cross correlation provides a tighter upper limit on $\Omega_{\text{gw}} h^2_{100}$ than that obtained from a single detector by a factor $\gamma_{\text{rms}} \sqrt{T \Delta_{\text{BW}}}$, where Δ_{BW} is the bandwidth over which the integrand of Equation 31 is significant, and where γ_{rms} is the rms value of $\gamma(f)$ over this bandwidth. For the H2-L1 correlation, this factor is of order several hundred.

Cross correlations were generated in 900-s intervals, which were short enough to account for nonstationary detector noise. The analysis was done in the frequency domain to facilitate the optimal filtering. Careful attention was paid to the windowing of the time-series data before the application of the Fourier transform to prevent the leakage of low-frequency components into the measurement band.

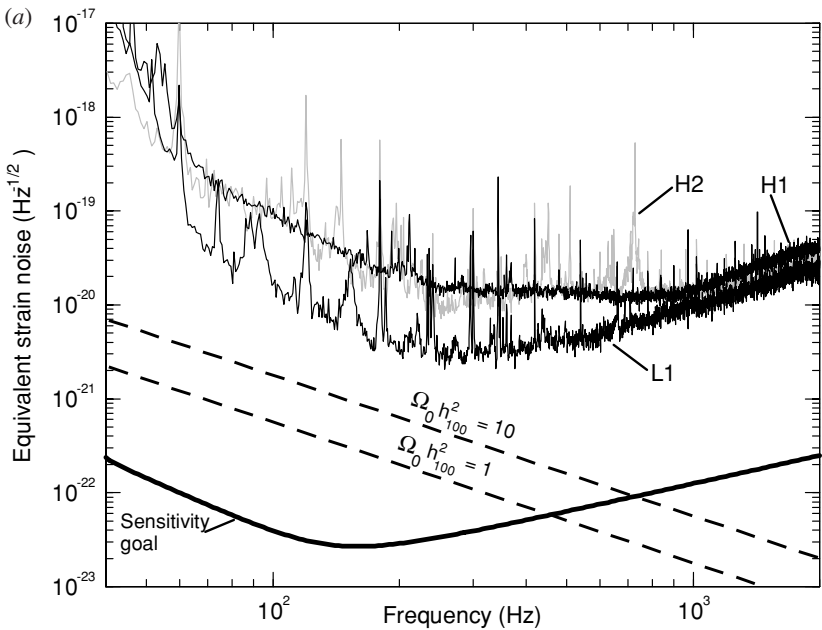


Figure 18 Search for stochastic background of gravitational waves. (a) Expected strain signals for stochastic backgrounds of 10 and 1. (b) Measured correlations of H2-L1 and H1-H2 detectors. The dashed lines show the expected correlation for $\Omega = 23$ and $\Omega = -8$, respectively. The correlation for H1-H2 detectors, both located at LIGO's Hanford observatory (LHO), is due to common environmental noise. (From Reference 130 with permission.)

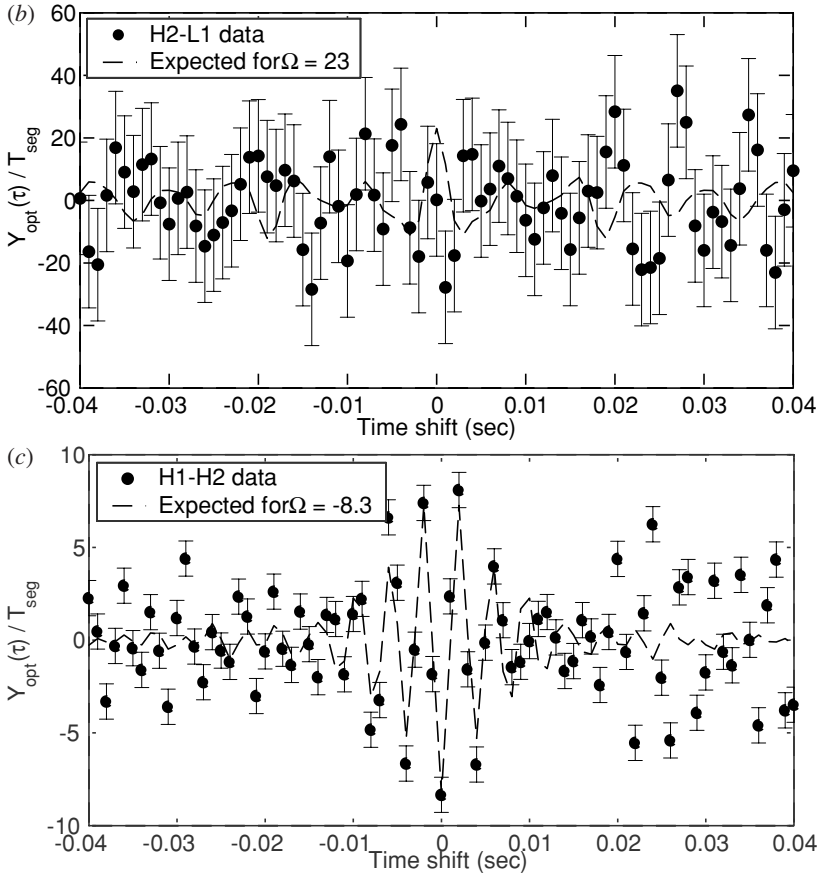


Figure 18 (Continued)

The upper limit (90% CL) set by the S1 analysis was $\Omega_0 h^2_{100} < 23$ in the frequency band 40–314 Hz. The cross-correlation results were examined through a time-shift analysis of the time-series data, shown for the H2-L1 and H1-H2 correlations in Figure 18*b,c*. (Time-shifting the data will remove a true correlation between the detectors.) The dashed lines show the expected correlations in the presence of a stochastic background with $\Omega_{\text{gw}}(f) = \text{constant}$. The H2-H1 data show an instrumental correlation, due possibly to common acoustic or seismic noise. The H2-L1 data are consistent with noise.

The upper limit was a factor of 10^4 improvement over the best previous broadband interferometric result. It is, however, large compared to the limit from big bang nucleosynthesis of $< 10^{-5}$.

4.2.4. PERIODIC WAVES FROM PSR J1939+2134 A search was undertaken for gravitational wave emission from the known pulsar J1939+2134 at its expected 1284 Hz

emission frequency (twice the pulsar frequency) (131). This pulsar has a rotational period of 1.6 ms and is 3.6 kpc from the earth.

The signal-to-noise ratio for a source of known frequency f_s will increase as the square root of the time T ; the amplitude h_0 of the signal that can be detected with 90% confidence, but would arise randomly from the Gaussian noise background only 1% of the time, is given by

$$h_0 = 11.4\sqrt{S_n(f_s)/T}, \quad 37.$$

where $S_n(f)$ is the noise power spectral density. For the ~ 200 h of data collection of the S1 run, this amplitude is $\sim 10^{-22}$ at 1284 Hz. In contrast, an upper limit of $h \sim 10^{-27}$ for this pulsar can be obtained, assuming the observed spindown rate is due solely to gravitational wave emission from this pulsar. Thus, a detection was not expected.

The data were heterodyned at the signal frequency, then low-pass filtered to suppress contamination from strong signals elsewhere in the detector band. An additional heterodyne was applied to account for the time-varying Doppler shift from the earth's rotation and orbit and spindown of the pulsar. An upper limit at 90% CL for the observed strain was found to be 1.5×10^{-22} for L1, the most sensitive detector. This in turn allowed a limit to be set on the neutron star's ellipticity: Using a value of 10^{45} g cm² for the star's moment of inertia, we find $\varepsilon < 2.9 \times 10^{-4}$.

4.3. Resonant Mass Detector (Bar) Results

The International Gravitational Event Collaboration (IGEC) performed a study of the results of the observations of the ALLEGRO, AURIGA, EXPLORER, NAUTILUS, and NIOBE cryogenic bar detectors during 1997–2000 (132). The search was focused on burst waves around the bars' resonant frequency of ~ 900 Hz. The detectors were oriented to be nearly parallel to maximize the probability of coincident signal detection. Each group independently conducted a burst search using an optimal filter and an adaptive threshold. Candidate events at $\text{SNR} > 3$ –5 (the threshold chosen to impose a background rate of $\sim 100/\text{day}$) were described by the peak amplitude, time of occurrence, and their uncertainties. This threshold would correspond to an energy of $\sim 0.1 M_s$ converted into a gravitational wave millisecond burst at a distance of 10 kpc. The accidental coincidence rate over a detection interval of 1 s (limited by a detection bandwidth of 1 Hz) was several per week for two detectors and several per century for three detectors.

No evidence for gravitational wave bursts was found. Coincidences between the detectors were well accounted for by the estimated background. Figure 19 shows an upper limit for the rate of the bursts as a function of burst amplitude threshold H_t . Because the time resolution of the data was not sufficient to resolve the incident wave direction, no directional search has been applied. A separate analysis of EXPLORER and NAUTILUS data taken over 90 days in 2001 did include directional information (133). A small excess in the number of coincidences was reported, corresponding to times when the detectors were favorably oriented with

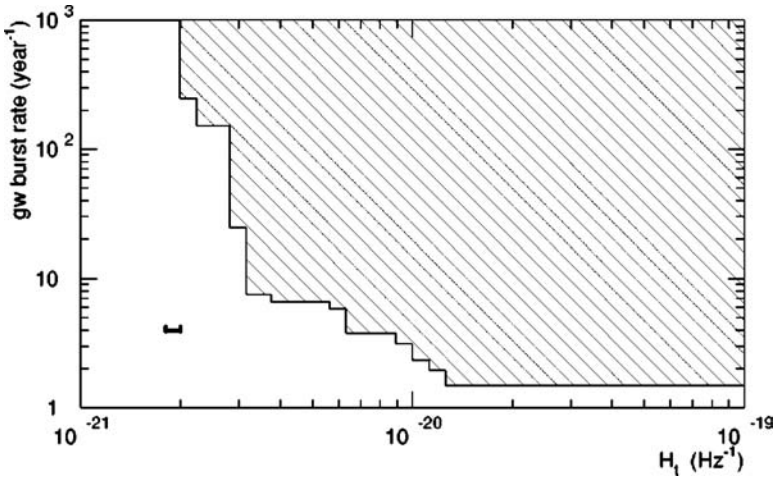


Figure 19 Upper limit for bursts from resonant bar collaboration. The results at each threshold value are cumulative and apply to bursts whose amplitudes are greater than H_t . (From Reference 132 with permission.)

respect to the galactic disc, but the level was too low to warrant any claim of an actual detection.

4.4. Doppler Tracking Results

In the past decade the Ulysses and Cassini spacecraft have been operated for the exploration of the sun and Saturn, respectively. On both missions, Doppler tracking set limits on gravitational waves in the 10^{-6} Hz to 10^{-4} Hz range.

Fourteen days of data were analyzed from Ulysses in 1992 (134), with a round-trip travel time of ~ 4400 s. Two different downlink carriers were used to attenuate the effect of the interplanetary plasma on the signal. The data was analyzed to search for a hypothetical binary black hole system with central mass $2 \times 10^6 M_s$ at the galactic center. For an orbital period of order 10^{-4} s, an upper limit of 6000 M_s for the mass of the proposed companion black hole was established.

In the Doppler tracking of Cassini (135), a multilink radio system, involving two uplink and three downlink signals, was used to remove noise from the interplanetary plasma. Tropospheric scintillation was also attenuated with a radiometer-based calibration system on the tracking antenna. Data were analyzed from a 40 day period in late 2001, with a round-trip time of ~ 5800 s. Analysis of the data set an upper limit on the stochastic background as shown in Figure 20. An upper limit for Ω of $\sim 10^{-5}$ is set from the model of primordial nucleosynthesis, so the Cassini data represent only an upper limit for an astrophysical background in this frequency band. This result is ~ 1000 times better than previous Doppler measurement.

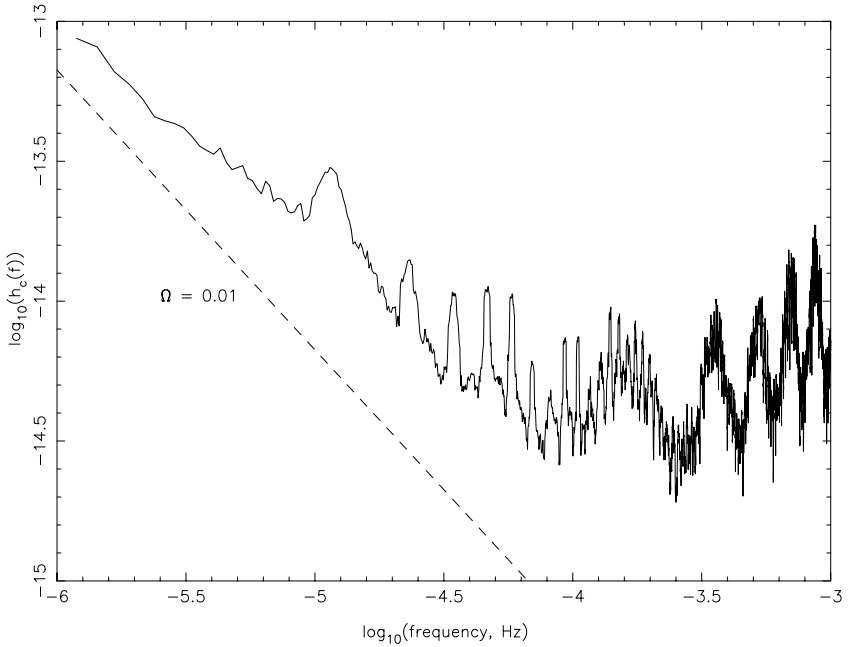


Figure 20 Strain sensitivity of Doppler tracking study of Cassini spacecraft. The expected signal from a stochastic background of $\Omega = 0.01$ is shown. (From Reference 134 with permission.)

4.5. Pulsar Timing Results

A number of pulsar timing measurements have been made to set limits on the existence of gravitational waves in the frequency range of 10^{-9} to 10^{-7} Hz.

Timing observations of the radio pulsar PSR B1855+09 have been examined for the imprint of gravitational waves with frequency 6×10^{-8} Hz, from a proposed supermassive binary black hole in galaxy 3C66B (136). Data from seven years of observations from the Arecibo Observatory were searched for fluctuations in the pulsar signal arrival times at the proposed emission frequency. The absence of such fluctuations ruled out the proposed system at a confidence level of 98%, given a total mass of $5 \times 10^{10} M_{\odot}$ and chirp mass of $1.3 \times 10^{10} M_{\odot}$, for an eccentricity of < 0.03 .

A search for a stochastic background of MBH coalescence was performed by examining pulses from the millisecond pulsar B1855+09 (137). This pulsar has been under observation by the Arecibo and Green Bank telescopes for a total of 17 years. No unexplained perturbations were found in the timing residuals, of order $10 \mu\text{s}$, setting an upper limit for the energy density in gravitational waves of $\Omega h^2_{100} < 2 \times 10^{-9}$.

4.6. Space-Based Interferometer Analysis

Although data from the first space-based interferometer, LISA, are not expected until the next decade, considerable work has already gone into exploring its measurement capabilities (138, 139). Efforts are now under way to develop and test data-analysis algorithms on simulated LISA data (140).

Signal analysis for space-based interferometers will employ many of the same techniques used to analyze data from ground-based interferometers—such as matched filtering and time-frequency plots—but the character of the data-analysis problems is very different. The high-frequency sources sought by ground-based detectors are mostly short-lived transients, whereas the low-frequency sources sought by space-based detectors are mostly long-lived and continuous. This difference in source duration has two main consequences. The first is that the high-frequency signals will tend to be isolated in time while the low-frequency signals overlap in time; the second is that orbital motion of the detector is unimportant for ground-based detectors but is essential for locating sources with space-based detectors. The main data-analysis challenge for LISA will be identifying individual sources from a data stream that contains tens of thousands of overlapping sources (141).

During the course of a year, a typical LISA signal will complete tens of thousands of cycles. In order for a template to match the signal, the source parameters that control the phase evolution, such as the mass or orbital frequency, must

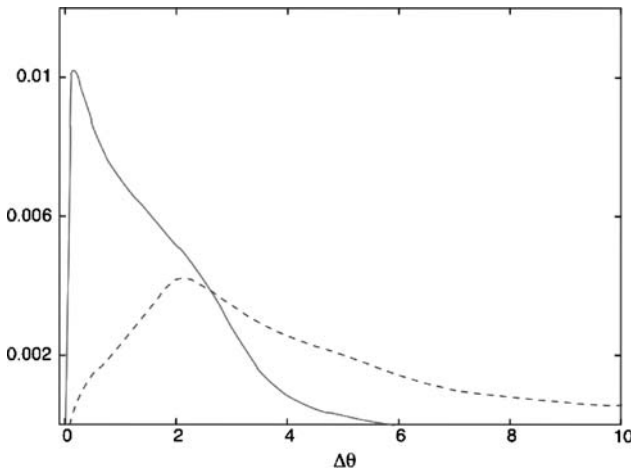


Figure 21 Histograms showing the angular resolution of the LISA detector in degrees for the brightest galactic sources after three years of observation (*solid line*), and for a population of black holes at redshift $z = 3$ observed over their final year of inspiral (*dashed line*). The galactic sources were selected from a realization of the galactic background with a brightness threshold of $\text{SNR} > 10$. The black holes were drawn from an all-sky distribution with a mass distribution uniform in $\log(M/M_\odot)$, and with a detection threshold of $\text{SNR} > 5$. (Figure contributed by Neil Cornish & Jeff Crowder.)

be known to high precision. In contrast, parameters that control the amplitude of the signal—such as the distance to the source, the orbital inclination, and polarization—need only be known to low precision. Directional information comes from the antenna pattern being swept across the sky and from the time-dependent Doppler shift as LISA moves toward, then away from, a source. The accuracy with which the source parameters can be determined is inversely proportional to the signal-to-noise ratio and strongly depends on the source parameters themselves. Figure 21 shows the distribution of angular resolutions for bright galactic sources, along with the distribution of angular resolutions for a population of MBH binaries at redshift $z = 3$ (corresponding to a luminosity distance of 25 Gpc). The median values for the angular resolution are 1.4 and 3.7° , respectively. Other source parameters are determined to varying degrees of precision; for the black hole population, the median fraction errors in the individual masses are $\sim 10^{-3}$, the time to coalescence is 10^{-5} , and the luminosity distance is 0.3 .

5. CONCLUSIONS

There is strong reason for optimism in the gravitational wave community.

At the time of this writing, the LIGO H1 detector has reached within a factor of three of its design sensitivity across its full detection band between 80 and 1000 Hz (R. Weiss, private communication). Work is under way to upgrade the seismic isolation system to enable the detectors' duty cycles to approach 100%. It is expected that after the end of 2004, all three LIGO detectors will be operating at full design sensitivity, and that a year-long data run can then begin. At full sensitivity, LIGO will have a reach for a neutron binary inspiral that will extend to the Virgo cluster, accessing hundreds of galaxies. Equally important to the achievement of its designed detection range, LIGO has demonstrated that the physics and engineering of interferometry is well understood and predictable at the 10^{-18} m rms level. This has already led to the start of research and development of the technology necessary for LIGO's next-generation detector, which will provide at least a tenfold increase in detection range and a corresponding detection rate increase of ~ 1000 -fold.

The addition of the GEO and VIRGO detectors at full design sensitivity within the next few years will establish gravitational wave astronomy as a truly international effort. The simultaneous operation of geographically separated detectors will enable source localization and facilitate optimization to particular source frequencies.

Space-based interferometry is also under active development. The LISA project, a NASA/ESA collaboration, is now engaged in the technology development of space interferometry and drag-free spacecraft control to open up the 10^{-4} Hz to 10^{-1} Hz measurement band. A test flight to demonstrate the technology of drag-free control is scheduled for 2007, and the launch of LISA is scheduled for 2013.

Finally, as the experimentalists continue to develop their detection hardware, the understanding of potential gravitational wave sources has also advanced. For example, the recent discovery of a 22 ms pulsar has increased by an order of

magnitude the expected event rate for neutron binary inspiral detection by the initial LIGO, so that one event per year is now plausible (54).

Observation within the coming decade of even some of the gravitational wave sources described in this article will bring a wealth of new information and perspective to our understanding of the universe. History shows that the opening of a new observational window brings surprises and insights of a kind not dreamt of in our philosophy. We expect that the realization of gravitational wave astronomy will be no exception.

ACKNOWLEDGMENTS

We thank our many colleagues who have participated with us in this exciting enterprise, too numerous to mention individually. Special thanks for comments on this manuscript to Sam Finn, Curt Cutler, Albert Lazzarini, and Peter Bender.

**The Annual Review of Nuclear and Particle Science is online at
<http://nucl.annualreviews.org>**

LITERATURE CITED

1. Einstein A. *Ann. Physik* 17 (1905)
2. Einstein A, Grommer J. *Sitzber. Deut. Akad. Wiss. Berlin* 2 (1927)
3. Dixon W. *Transact. R. Soc. London A* 277:59 (1974)
4. Detweiler S, Whiting B. *Phys. Rev. D* 67:024025 (2003)
5. Einstein A. *K. Preuss. Akad. Wiss.* 1916:688 (1916)
6. Einstein A. *K. Preuss. Akad. Wiss.* 1918:154 (1918)
7. Einstein A, Rosen NJ. *Franklin Inst.* 223:43 (1937)
8. Landau L, Lifshitz E. *Classical Theory of Fields*. Reading, MA: Addison-Wesley (1962)
9. Pirani F. In *Conference on the Role of Gravitation in Physics, Proc. Conf. at Chapel Hill, North Carolina*, ed. CM De Witt, p. 37. Wright Air Development Center Tech. Rep. 57-216, US Air Force, Wright-Patterson Air Force Base, OH (1957)
10. Taylor J. *Rev. Mod. Phys.* 66:711 (1994)
11. Kennefick D. In *The Expanding Worlds of General Relativity (Einstein Studies, Vol. 7)*, ed. H Goenner, J Renn, J Ritter, T Sauer, p. 207. Boston: Birkhauser (1999)
12. Weber J. *Phys. Rev. Lett.* 17:1228 (1966)
13. Weber J. *Phys. Rev. Lett.* 22:1320 (1969)
14. Moss GE, et al. *Appl. Opt.* 10:2495 (1971)
15. Weiss R. *MIT RLE Q. Prog. Rep.* 105:54 (1972)
16. Forward R. *Phys. Rev. D* 17:379 (1978)
17. Abramovici, et al. *Phys. Lett.* A218:157 (1996)
18. Robertson, et al. *Rev. Sci. Instrum.* 66:4447 (1995)
19. Shoemaker D, et al. *Phys. Rev. D* 38:423 (1988)
20. Faller J, Bender P. In *Second Int. Conf. Precision Measurements and Fundamental Constants*. Gaithersburg, MD: Natl. Bur. Standards (1981)
21. Misner C, Thorne K, Wheeler J. *Gravitation*. New York: W. H. Freeman (1971)
22. Schutz B. *Proc. Alpbach Summer School*, ed. A Wilson, p. 229. Eur. Space Agency Pub. SP-420 (1997)
23. Schutz B. *Nature* 323:310 (1986)

24. Schutz B. *A First Course in General Relativity*. Cambridge, UK: Cambridge Univ. Press (1995)
25. Weinberg S. *Gravitation and Cosmology*. New York: Wiley (1972)
26. Finn L, Thorne K. *Phys. Rev. D* 62:124021 (2000)
27. Barack L, Ori A. *Phys. Rev. Lett.* 90: 111101 (2003)
28. Baumgarte T, Shapiro S. *Phys. Rep.* 376:41 (2003)
29. Choi D, et al. *J. Comp. Phys.* 193:398 (2004)
30. Luc Blanchet. *Living Rev. Rel.* 5:3 (2002)
31. Abbott L, Wise M. *Nucl. Phys B* 244:541 (1984)
32. Kamionkowski M. *Int. J. Mod. Phys. A* 16:116 (2001)
33. Nicolis A. *Class. Quant. Grav.* 21:L27 (2004)
34. Bender P, Hils D. *Class. Quant. Grav.* 14:1439 (1997)
35. Cooray A, Farmer A, Seto N. *Ap. J.* 601:L47 (2004)
36. Cutler C, Hiscock W, Larson S. *Phys. Rev. D* 67:024015 (2003)
37. Schodel R, et al. *Nature* 419:694 (2002)
38. Rees M. *Class. Quant. Grav.* 14:1411 (1997)
39. Quinlan G, Shapiro S. *Astrophys. J.* 356:483 (1990)
40. Milosavljevic M, Merritt D. *Astrophys. J.* 596:860 (2003)
41. Kokkotas K, Schmidt B. <http://www.livingreviews.org/lrr-1999-2> (1999)
42. Dreyer O, et al. *Class. Quant. Grav.* 21: 787 (2004)
43. Haehnel M. *Mon. Not. R. Astron. Soc.* 269:199 (1994)
44. Ryan F. *Phys. Rev. D* 52:5707 (1995)
45. Barack L, Cutler C. *Phys. Rev. D* 69:082005 (2004)
46. Hughes S. *Phys. Rev. D.* 64: 064004 (2001)
47. Sigurdsson S, Rees M. *Mon. Not. R. Astron. Soc.* 284:318 (1997)
48. New K, Shapiro S. *Astrophys. J.* 548:439 (2001)
49. Turner M. *Phys. Rev. D* 55:435 (1997)
50. Caldwell B, Allen B. *Phys. Rev. D* 45:3447 (1992)
51. Hogan C. *Class. Quant. Grav.* 18:4039 (2001)
52. Kolb E, Turner M. *The Early Universe*. Reading, MA: Addison-Wesley (1990)
53. Cutler C, Thorne K. In *General Relativity and Gravitation*, ed. NT Bishop, SD Maharaj, p. 72. Singapore: World Sci. (2002)
54. Burgay M, et al. *Nature* 426:531 (2003)
55. Nutzman P, et al. astro-ph/0402091
56. Grandclément, et al. *Phys. Rev. D* 67: 042003 (2003)
57. Cutler C, Flanagan E. *Phys. Rev. D* 49: 2658 (1994)
58. Faber J. *Phys. Rev. Lett.* 89:231102 (2002)
59. Ushomirsky U, et al. *Mon. Not. R. Astron. Soc.* 319:902 (2000)
60. Cutler C. *Phys. Rev. D* 66:084025 (2002)
61. Muller E, et al. astro-ph/0309833
62. Saijo M, et al. *Astrophys. J.* 548:919 (2001)
63. Meszaros P. *Annu. Rev. Astron. Astrophys.* 40:529 (2000)
64. Dimmelmeier H. *Astrophys. J. Lett.* 560:L163 (2001)
65. Meszaros P, et al. *New Astron.* 4:303 (1999)
66. Kobayashi S, Meszaros P. *Astrophys. J.* 589:861 (2003)
67. Fryer C, Warren M. *Astrophys. J.* 601:391 (2004)
68. Finn S, Mohanty S. *Phys. Rev. D* 60:12110 (1999)
69. Gehrels N, et al. *Astrophys. J.* (2004)
70. Grishchuk L. *Sov. Phys. JETP* 40:409 (1974)
71. Maggiore M. *Phys. Rep.* 331:283 (2000)
72. Hogan C. *Phys. Rev. Lett.* 85:2044 (2000)
73. Callen H, Welton T. *Phys. Rev.* 83:34 (1951)
74. Berger J. *J. Geophys. Res.* 79:1210 (1974)
75. Thorne K, et al. *Phys. Rev. D* 58:122002 (1998)
76. Paik H. *J. Appl. Phys.* 47:1168 (1976)
77. Drever R, et al. In *Quantum Optics, Experimental Gravity and Measurement*

- Theory*, ed. P Meystre, M Scully, p. 503. New York: Plenum (1983)
78. Estabrook F, Wahlquist H. *Gen. Relativ. Gravit.* 6:439 (1975)
 79. Armstrong J. *Radio Sci.* 33:1727 (1998)
 80. Maucelli E, et al. *Phys. Rev. Lett.* 54:1264 (1996)
 81. Prodi G, et al. *Proc. 2nd Edoardo Amaldi Conf. Gravitational Waves*, ed. E Coccia, G Veneziano, P Pizzella, p. 148. Singapore: World Sci. (1999)
 82. Astone P, et al. *Phys. Rev. D* 47:362 (1993)
 83. Astone P, et al. *Astropart. Phys.* 7:231 (1997)
 84. Blair D, et al. *Phys. Rev. Lett.* 74:1908 (1995)
 85. Coccia E. *Class. Quant. Grav.* 20:S135 (2003)
 86. Hamilton W. *AIP Conference Proceedings*, ed. J Centrella, 575:24. New York: AIP (2000)
 87. Abramovici A, et al. *Science* 256:325 (1992)
 88. Barish B, Weiss R. *Phys. Today* 52:44 (1999)
 89. Savage R, et al. *Laser Phys.* 8:679 (1998)
 90. Rudiger A, et al. *Optica Acta* 28:641 (1981)
 91. Whitcomb S, et al. *Proc. TAMA Int. Workshop Gravitational Wave Detection*, ed. K Tsubono, M Fujimoto, K Kuroda, p. 229. Tokyo: Universal Acad. Press (1997)
 92. Camp J, et al. *Proc. 2nd TAMA Int. Workshop Gravitational Wave Detection*, ed. S Kawamura, N Mio, p. 279. Tokyo: Universal Acad. Press (2000)
 93. Regehr M, et al. *Opt. Lett.* 20:1507 (1995)
 94. Fritschel P, et al. *Appl. Opt.* 40:4988 (2001)
 95. Fritschel P, et al. *Appl. Opt.* 37: 6734 (1998)
 96. Drever R, et al. *Appl. Phys.* B31:97 (1983)
 97. Giaime J, et al. *Rev. Sci. Instrum.* 74:218 (2003)
 98. Acernese F, et al. *Class. Quant. Grav.* 19:1421 (2002)
 99. Ballardín G, et al. *Rev. Sci. Instrum.* 72:3643 (2001)
 100. Danzmann K, et al. *Proc. 1st Edoardo Amaldi Conf. Gravitational Wave Experiments*, ed. E Coccia, G Pizzella, F Ronga, p. 100. Singapore: World Sci. 1995)
 101. Meers B. *Phys. Rev. D* 38:2317 (1988)
 102. Plissi M, et al. *Rev. Sci. Instrum.* 71:2539 (2000)
 103. Ando M, et al. *Class. Quant. Grav.* 19: 1409 (2002)
 104. Astrium et al. ESTEC Rep. No. LI-RP-DS-009 (2000)
 105. Danzmann K. LISA Pre-Phase A Rep. MPQ-233, Max-Planck Inst. Quantenoptik, Garching, Ger. (1998)
 106. Armstrong J, et al. *Class. Quant. Grav.* 20: S283 (2003)
 107. Bortoluzzi D, et al. *Class. Quant. Grav.* 20:S89 (2003)
 108. Schumaker B. *Class. Quant. Grav.* 20: S239 (2003)
 109. Camp J, et al. *J. Appl. Phys.* 71:783 (1992)
 110. Carbone et al. *Phys. Rev. Lett.* 91: 151101 (2003)
 111. Deleted in proof
 112. Coccia E, et al. *Phys. Rev. D* 52:3735 (1995)
 113. de Waard A. *Class. Quant. Grav.* 20:S143 (2002)
 114. Fritschel P. *Gravitational Wave Detection, Proc. SPIE* 4856:282. Bellingham, WA: SPIE (2003)
 115. Uchiyama T. *Class. Quant. Grav.* 21: S1161 (2004)
 116. Ohashi M, et al. *Class. Quant. Grav.* 20:S599 (2003)
 117. Deleted in proof
 118. Deleted in proof
 119. Wainstein L, Zubakov V. *Extraction of Signals from Noise*. Englewood Cliffs, NJ: Prentice-Hall (1962)
 120. Blanchet L, et al. *Class. Quant. Grav.* 13:575 (1996)
 121. Anderson W, et al. *Phys. Rev. D* 63: 042003 (2001)
 122. Sylvestre J. *Phys. Rev. D* 66:102004 (2002)

123. Smith A. *Biometrika* 62:407 (1975)
124. Saulson P. *Fundamentals of Interferometric Gravitational Wave Detectors*. Singapore: World Sci. (1994)
125. Backer D, et al. In *Carnegie Observatories Astrophysics Series*, Vol. 1. Pasadena, CA: Carnegie Observatories (2003)
126. Abbott B, et al. *Nucl. Inst. Methods A* 517:154 (2004)
127. Deleted in proof
128. Abbott B, et al. (LIGO Sci. Collab.) *Phys. Rev. D* 69:102001 (2004)
129. Abbott B, et al. (LIGO Sci. Collab.) *Phys. Rev. D* 69:122001 (2004)
130. Abbott B, et al. (LIGO Sci. Collab.) *Phys. Rev. D* 69:122004 (2004)
131. Abbott B, et al. (LIGO Sci. Collab.) *Phys. Rev. D* 69:082004 (2004)
132. Astone P, et al. *Phys. Rev. D* 68:022001 (2003)
133. Astone P, et al. *Class. Quant. Grav.* 19:5449 (2002)
134. Bertotti B, et al. *Astron. Astrophys.* 296:13 (1995)
135. Armstrong J, et al. *Astrophys. J.* 599:806 (2003)
136. Jenet F, et al. astro-ph/0310276 *Astrophys. J.* 606:799 (2004)
137. Lommen A. astro-ph/0208572
138. Cutler C. *Phys. Rev. D* 57:07089 (1998)
139. Takahashi R, Seto N. *Astrophys. J.* 575:1030 (2002)
140. Rubbo L, Cornish N, Poujade O. *AIP Conf. Proc.*, ed. J Centrella, 686:307. New York: AIP (2003)
141. Cornish N, Larson S. *Phys. Rev. D* 67:103001 (2003)

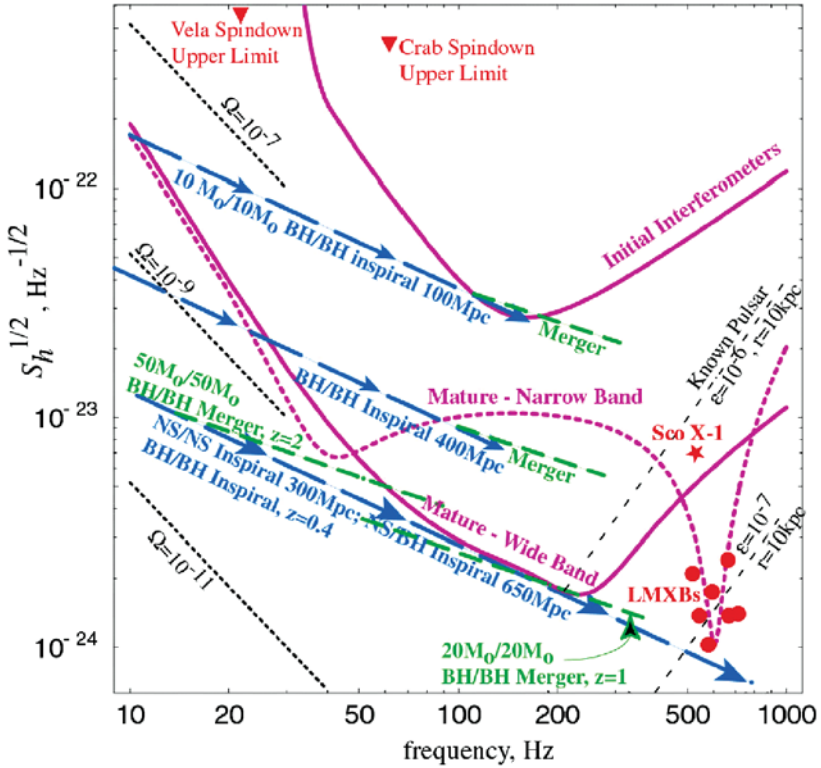


Figure 5 Gravitational wave sources sought by LIGO. Also shown are the sensitivity curves of the initial and advanced LIGO interferometers. The advanced LIGO sensitivity is shown tuned to the known frequency of an x-ray binary (see Section 3). (From Reference 53 with permission.)

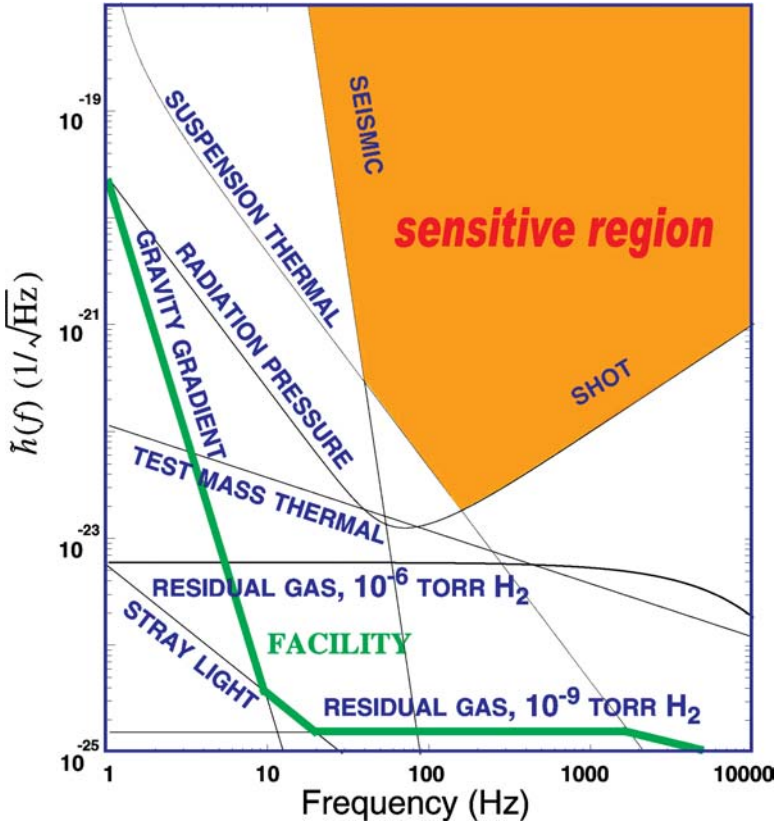


Figure 9 LIGO noise curves, including seismic, thermal, shot, radiation pressure, residual gas, gravity gradient, and total noise.

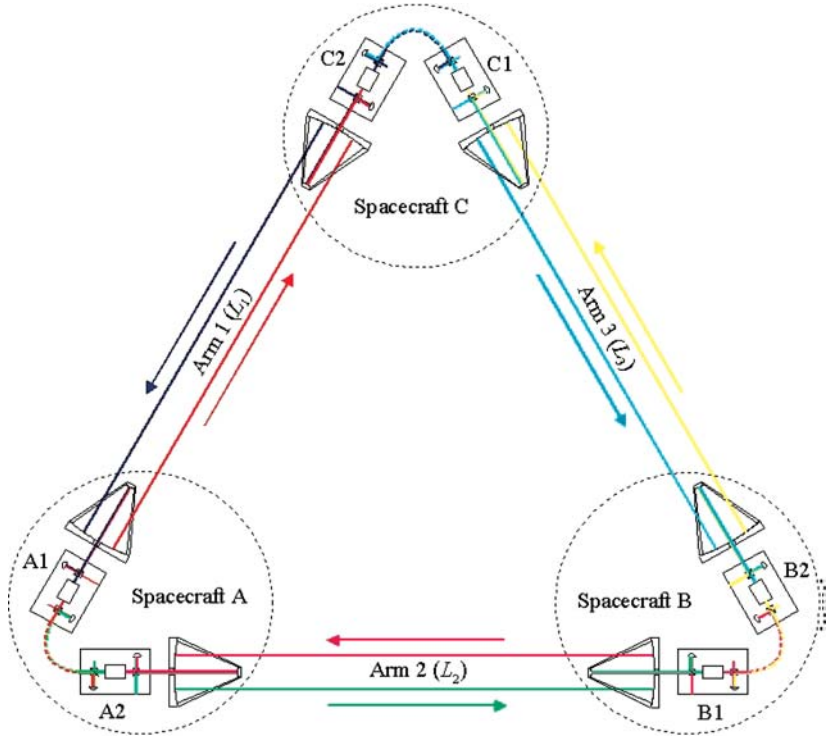


Figure 11 LISA constellation. On each spacecraft lasers are phase locked, and each spacecraft transmits and receives light from each of its neighbors.

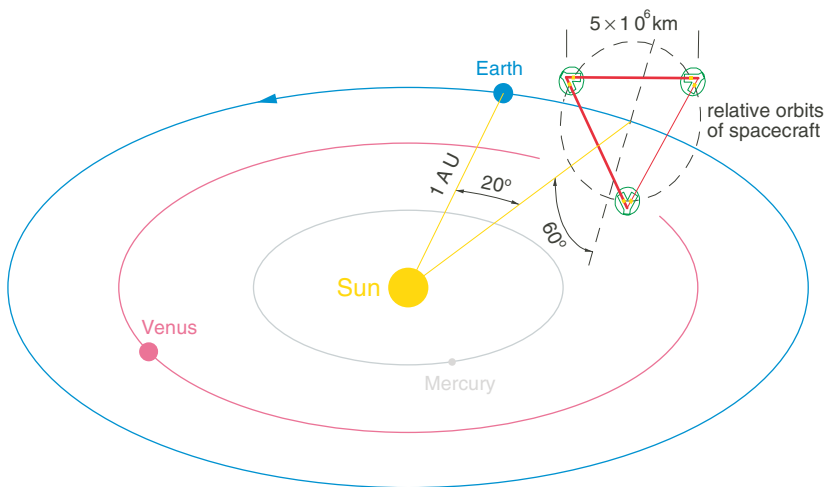


Figure 12 Orbit of LISA constellation. The constellation triangle rotates once per year.

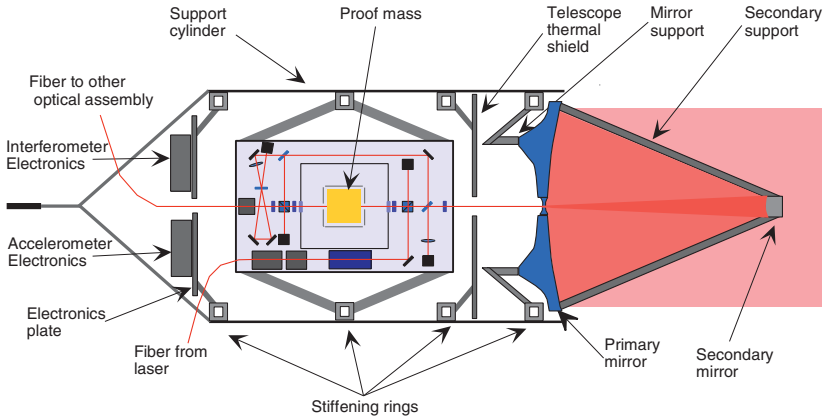


Figure 13 LISA optical assembly. Light from an external laser is brought to the bench with a fiber, reflected from the proof mass, and expanded by the telescope.

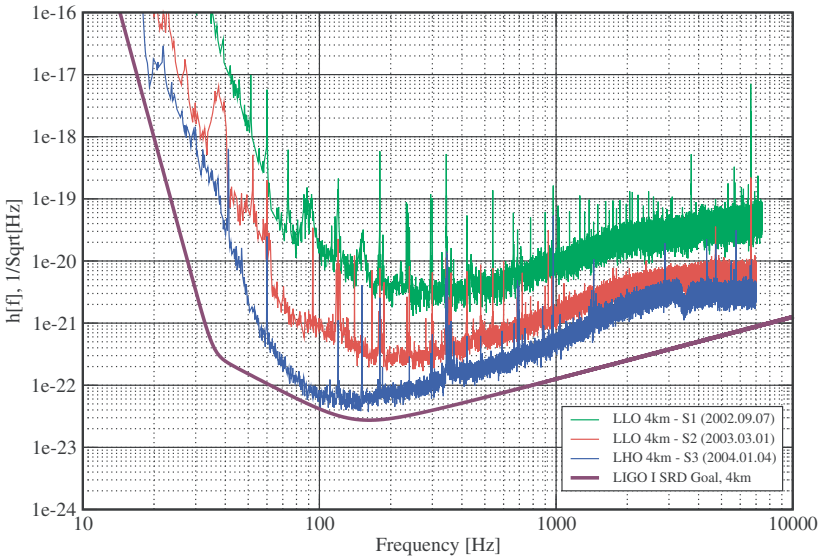


Figure 15 LIGO detector sensitivities during the S1, S2, and S3 runs. The analyses described in this article used data from the S1 run.

CONTENTS

FRONTISPIECE, <i>Lincoln Wolfenstein</i>	xii
THE STRENGTH OF THE WEAK INTERACTIONS, <i>Lincoln Wolfenstein</i>	1
THE SOLAR <i>hep</i> PROCESS, <i>Kuniharu Kubodera and Tae-Sun Park</i>	19
TRACING NOBLE GAS RADIONUCLIDES IN THE ENVIRONMENT, <i>Philippe Collon, Walter Kutschera, and Zheng-Tian Lu</i>	39
THE GERASIMOV-DRELL-HEARN SUM RULE AND THE SPIN STRUCTURE OF THE NUCLEON, <i>Dieter Drechsel and Lothar Tiator</i>	69
THE THEORETICAL PREDICTION FOR THE MUON ANOMALOUS MAGNETIC MOMENT, <i>Michel Davier and William J. Marciano</i>	115
THE BROOKHAVEN MUON ANOMALOUS MAGNETIC MOMENT EXPERIMENT, <i>David W. Hertzog and William M. Morse</i>	141
THE NUCLEAR STRUCTURE OF HEAVY-ACTINIDE AND TRANSACTINIDE NUCLEI, <i>M. Leino and F.P. Heßberger</i>	175
ELECTROMAGNETIC FORM FACTORS OF THE NUCLEON AND COMPTON SCATTERING, <i>Charles Earl Hyde-Wright and Kees de Jager</i>	217
PHYSICS OPPORTUNITIES WITH A TEV LINEAR COLLIDER, <i>Sally Dawson and Mark Oreglia</i>	269
DIRECT DETECTION OF DARK MATTER, <i>Richard J. Gaitskell</i>	315
BACKGROUNDS TO SENSITIVE EXPERIMENTS UNDERGROUND, <i>Joseph A. Formaggio and C.J. Martoff</i>	361
GENERALIZED PARTON DISTRIBUTIONS, <i>Xiangdong Ji</i>	413
HEAVY QUARKS ON THE LATTICE, <i>Shoji Hashimoto and Tetsuya Onogi</i>	451
THE GRIBOV CONCEPTION OF QUANTUM CHROMODYNAMICS, <i>Yuri L. Dokshitzer and Dmitri E. Kharzeev</i>	487
GRAVITATIONAL WAVE ASTRONOMY, <i>Jordan B. Camp and Neil J. Cornish</i>	525

INDEXES

Cumulative Index of Contributing Authors, Volumes 45–54	579
Cumulative Index of Chapter Titles, Volumes 45–54	582

ERRATA

An online log of corrections to *Annual Review of Nuclear and Particle Science* chapters may be found at
<http://nucl.annualreviews.org/errata.shtml>